TWO-PHASE OPERATIONAL PERFORMANCE OF A TERRY GS-2 STEAM TURBINE USING AIR & WATER AS WORKING FLUIDS

A Thesis

by

JOSHUA ANDREW VANDERVORT

Submitted to the Office of Graduate and Professional Studies of
Texas A&M University
in partial fulfillment of the requirements for the degree of

MASTER OF SCIENCE

Chair of Committee,	Adolfo Delgado-Marquez
Committee Members,	Karen Vierow Kirkland
	Jonathan Felts
Head of Department,	Andreas A. Polycarpou

May 2020

Major Subject: Mechanical Engineering

ABSTRACT

This project investigates the performance of a Terry GS-2 turbine, and the attached trip-throttle valve and governor valve under two-phase (air/water) flow conditions. Because of their robust design, Terry turbines are used within the nuclear power generation industry in Reactor Core Isolation Cooling (RCIC) systems to remove decay heat during isolation events. During the Fukushima Daiichi nuclear power station disaster in Japan in 2011, the RCIC system and associated Terry turbine operated for over 70 hours: much longer than the 8 - 12 hours typically expected of similar RCIC systems, as they are expected to over-speed and trip upon backup battery depletion and loss of flow control. Theories suggest the turbine was subjected to a two-phase flow, thus degrading the turbine performance, while the RCIC system was simultaneously experiencing conditions that promoted self-regulating operation.

The project experimentally determines the flow coefficient of the two valves when subjected to single-phase air and single-phase water flow conditions over the range of valve stem withdrawal positions. The project also investigates the effect of inlet pressure, flow quality (air mass fraction), and turbine rotational speed on the performance of the turbine when subject to two-phase flows. The turbine was tested at inlet pressures ranging from 20 to 70 psia, qualities from 100% (single-phase air) to 5%, and rotational speeds up to 3600 RPM. The turbine performance is evaluated using torque and efficiency variation as a function of two-phase flow.

A flow visualization study was included to better understand the interaction between the gaseous and liquid phases of the two-phase flow, especially at elevated pressures within

the turbine nozzles. The two-phase flow regimes are characterized as a function of pressure and flow quality. Preliminary data regarding the turbine bearing friction is also discussed.

The results will be combined with previous data from a small-scale Terry ZS-1 steam turbine to understand the scaling relationship between large and small Terry turbines. Experimental data and analysis will assist investigators in understanding the performance of the Terry turbine as a component of the RCIC system, and provide experimental data for the validation of turbine models simulating the Fukushima accident.

ACKNOWLEDGEMENTS

There are many people who I would like to thank and acknowledge for helping me throughout my educational journey, particularly in graduate school. First and foremost, I would like to thank my research advisor, Dr. Adolfo Delgado, and research engineer, Dr. Abhay Patil, for this research opportunity and for their guidance and support throughout graduate school. I would like to also thank Dr. Karen Vierow Kirkland of Texas A&M and Matthew Solom of Sandia National Laboratories for their organization and leadership of the project at Texas A&M.

Numerous others provided valuable outside technical support, including, Doug Osborn, Chan Patel, Randy Bunt, Nobuyoshi Tsuzuki, Lynn Revak, Lendell Keene, BJ Keene, and Richard Mullins. The previous segments of this program were led by Nick Luthman, Yintao Wang, Ashraf Alfandi, and Shaym Balasubramanian. Gavin Lukasik provided invaluable assistance throughout much of the project. I'd like to also thank many of the students at the Texas A&M Turbomachinery Laboratory who provided great company throughout my graduate studies.

Lastly, I would like to thank my parents, Kurt and Cindy, as well as my brother, Kaleb, for all of their love and support throughout my studies. I would not have been able to complete my Master's degree without their listening ears and gentle encouragement.

CONTRIBUTORS AND FUNDING SOURCES

This work was supervised by a thesis committee consisting of Professor Adolfo Delgado and Professor Jonathan Felts of the Department of Mechanical Engineering and Professor Karen Vierow Kirkland of the Department of Nuclear Engineering. Dr. Abhay Patil of the Texas A&M Turbomachinery Laboratory provided additional support.

Sandia National Laboratories provided technical assistance throughout the project. The main test article, the Terry turbine and associated valves, was on loan from Pooled Inventory Management (PIM) of Southern Company. This project is part of an experimental and analytical program, at Texas A&M University, to characterize Terry turbine performance under two-phase flow. The program at Texas A&M University, is part of a larger program, to model and understand RCIC system behavior during the Fukushima Daiichi nuclear power station accident. Participants of this larger program include, the Institute of Applied Energy (Japan), the US Department of Energy, Sandia National Laboratories, Idaho National Laboratory, the Boiling Water Reactor Owners Group (BWROG) and others.

Undergraduate student, Gavin Lukasik, assisted throughout test loop construction and modification, data collection, and with the turbine performance uncertainty analysis. The student author completed all other work.

Financial support for this work was provided by the Institute of Applied Energy (IAE Japan).

NOMENCLATURE

Acronyms:

BDBE	Beyond Design Basis Event
BEP	Best Efficiency Point
GV	Governor Valve
IEC	International Electrotechnical Commission
RCIC	Reactor Core Isolation Cooling
RPV	Reactor Pressure Vessel
SBO	Station Blackout
TTV	Trip-Throttle Valve

Mathematical Symbols:

C_v	Flow Coefficient
M	Molar Mass
$\dot{m}$	Mass Flow Rate
n	Polytropic Constant (1.4 for air)
p	Absolute Pressure
p_1	Static Pressure Upstream of Valve Specimen
P_{gas}	Power Flowing into Turbine due to Gas Phase
P_{liquid}	Power Flowing into Turbine due to Liquid Phase
p_{inlet}	Turbine Inlet Static Pressure

p_{outlet}	Turbine Outlet Static Pressure
Q_g	Gas Phase Volume Flow Rate
Q_l	Liquid Phase Volume Flow Rate
R	Gas Constant
T	Absolute Temperature
T_1	Static Temperature Upstream of Valve Specimen
$\dot{V}$	Volume Flow Rate
$\dot{V}_{inlet}$	Turbine Inlet Gas Volume Flow Rate
$\dot{W}_{shaft}$	Turbine Shaft Output Power
x	Dimensionless Pressure Drop Across Valve Specimen
x_T	Pressure Differential Ratio Factor
Y	Compressibility Coefficient
YC	Compressible Flow Coefficient ($Y * C_v$)

Greek Letters:

Δp	Differential Pressure across Valve Specimen
η	Turbine Efficiency
ρ	Liquid Density
ρ_0	Reference Density of Water
τ	Turbine Output Torque
ω	Turbine Rotational Speed

TABLE OF CONTENTS

Page

LIST OF FIGURES

Page

LIST OF TABLES

Page

1. INTRODUCTION AND BACKGROUND

On March 11, 2011, there was a large earthquake beneath the Pacific Ocean off the coast of Japan. This magnitude 9.0 earthquake unleashed a large tsunami which inundated many coastal Japanese regions, particularly northeastern ones. Several nuclear power plants resided within the affected areas, most notably Fukushima Daiichi. The plant had to shut down unexpectedly upon the arrival of the tsunami. In the ensuing days, three of the six reactors at the main site melted down due to the loss of external power and damage from the flooding of the backup diesel generators, as auxiliary power is necessary to effectively operate cooling systems. One unit, unit 2, was damaged less severely than the others. In unit 2, it is believed the reactor core isolation cooling (RCIC) system was running for nearly 70 hours during the station blackout (SBO), thus mitigating the damage to the reactor and surrounding environment. This interval of operation greatly exceeds the 8 – 12 hours often attributed to other RCIC systems. The shorter operation period is based upon the assumption that the RCIC system fails after depletion of the backup battery, as the RCIC turbine is controlled by an electro-pneumatic system. Without power, the turbine is expected to activate the overspeed trip or ingest significant water through the steam lines to the point of losing functionality. Because of the SBO, the RCIC feedback and control mechanisms stopped regulating flow to the RCIC turbine, leading to unregulated operation for over 70 hours. It is believed that the RCIC system eventually failed due to significant water presence in the turbine oil and associated bearing failure from high suppression pool temperatures [1].

1.1. The RCIC System

The Reactor Core Isolation Cooling (RCIC) system is a safety-related standby system used for isolation events, but it is not considered an emergency cooling system [2]. As the name implies, the RCIC system is responsible for cooling the reactor core, while it is isolated from the main power generation turbines. The main components of the RCIC system include a steam turbine, water pump, and suppression chamber, a thermal reservoir partially filled with liquid water. When the main steam line isolation valve is closed, steam from the boiler is diverted away from the power generation turbines and into the RCIC turbine. After exiting the turbine, the expanded steam/water mixture fully condenses and cools in the suppression pool. The RCIC turbine powers the RCIC pump, which takes water from the suppression pool and returns it to the Reactor Pressure Vessel (RPV). The cooling water evaporates as it cools the core and is then sent back to the RCIC turbine, completing the loop. This process helps dissipate the fuel decay heat until another system comes online. Although RCIC was not originally designed for emergency shut down situations, the incident at Fukushima Daiichi demonstrated the system's ability to remove decay heat in emergency shut down situations for extended periods of time.

1.2. The Terry Turbine

The Terry Steam Turbine Company was founded in 1906 [3] and manufactured various steam turbines, which have been used in marine applications, petrochemical industry, and other industrial applications. These turbines have also been adopted for use in the RCIC system of nuclear power plants due to the turbine's robust design. They are

excellent candidates for use in nuclear safety systems which require resiliency and dependability in potentially harsh operating conditions, including two-phase flow. The robust design, however, comes at the expense of the turbine's operating efficiency. Therefore, these turbines are not used in nuclear power plants for electricity generation, which requires higher operating efficiencies.

The Terry steam turbines used in RCIC systems are impulse turbines, similar in design to the Pelton wheel. Figure 1 shows the turbine design. Steam enters the turbine and is directed to converging-diverging nozzles which accelerate the flow. The steam impinges on the buckets of the turbine wheel, transferring kinetic energy to the wheel. In the wheel, steam flow direction is reversed in the U-pattern bucket. Upon bucket exit, it enters a "reversing chamber" on the inner surface of the turbine casing, where the steam is reversed and sent back to the turbine wheel to deliver more kinetic energy. This looping pattern is performed 3-4 times until the steam has imparted all of its available kinetic energy to the wheel, at which point the steam exits the turbine at exit pressure. The left side of Figure 1 shows the steam's spiral flow pattern.

Under ideal (dry steam) operating conditions, the turbine behaves according to the characteristic curves provided by the manufacturer. However, when water is present, as is the case with two-phase flow, the expansion process across the nozzle may be significantly different from the ideal dry-steam case, and can degrade the turbine performance.

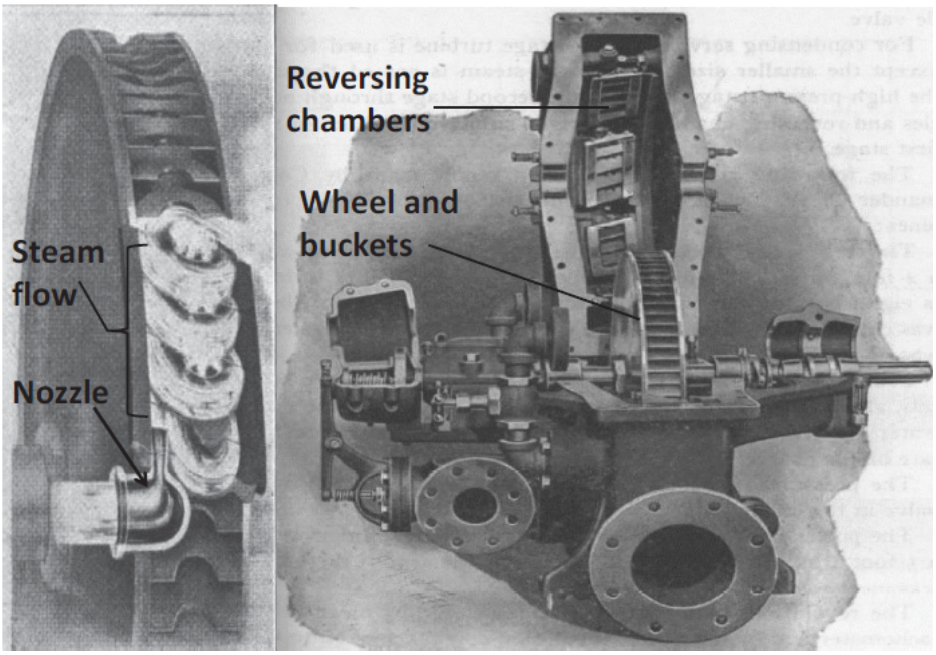

Figure 1: Terry Turbine Bucket Flow (Left) and Interior View of Turbine Case (Right). Adapted from [4]

Terry turbines are made in a variety of different models. The Terry ZS-series and GS-series turbines are made from steel and are suitable for steam use. A Terry turbine model GS-2 was used for this work. The GS-series turbines have 24-inch diameter wheels, while the ZS-series turbines have 18-inch diameter wheels. Nuclear power plants use either Terry GS-1 or GS-2 models in their RCIC systems. The GS-series turbines differ in the number of steam inlet nozzles. The Terry GS-1 turbine, the model employed at the Fukushima Daiichi power station at the time of the accident, has 5 steam inlet nozzles along the bottom half of the casing. On the other hand, the Terry GS-2 turbine used for these experiments has 10 steam inlet nozzles: 5 in the lower casing and 5 in the upper casing. The upper nozzles were plugged and only the lower 5 nozzles were used in testing, effectively mimicking a Terry

GS-1 configuration. Figure 2 shows two nozzles and reversing chambers installed on a Terry GS-2 turbine similar to the turbine that was used for this work.

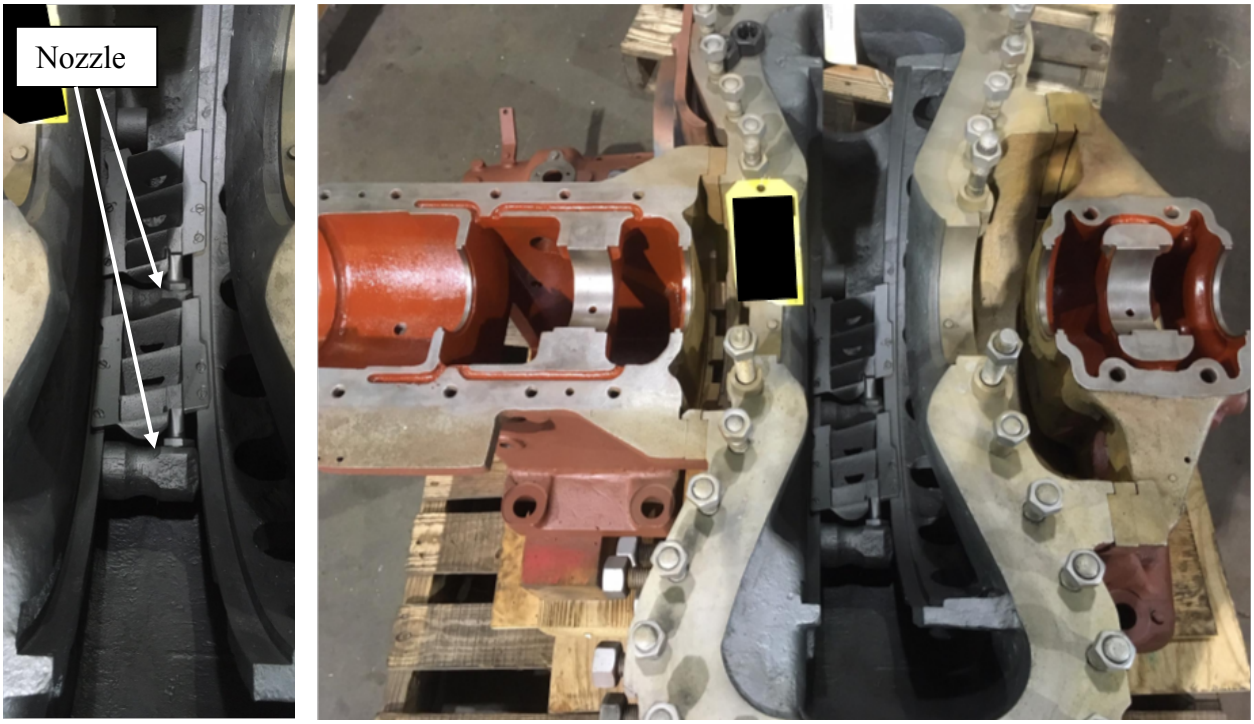

Figure 2: Terry GS-2 Turbine Lower Casing and Reversing Chambers

1.3. The Control Valves

In order to control the flow of steam to the RCIC turbine, two valves, a Trip/Throttle Valve (TTV) and a Governor Valve (GV) are connected immediately upstream of the turbine. The TTV is a Schutte & Koerting brand, 4" plug valve with a handwheel for controlling the valve position [5]. In practice, the TTV serves two functions. First, the valve is intended to act as a quick-closing emergency, or trip, valve if the turbine exceeds a set speed. Second, the valve assists with turbine start up by throttling the steam flow to the

turbine while bringing the turbine up to speed. The left side of Figure 3 shows a schematic of the test TTV, while the right side shows a newer drawing of the same model of valve from the manufacturer.

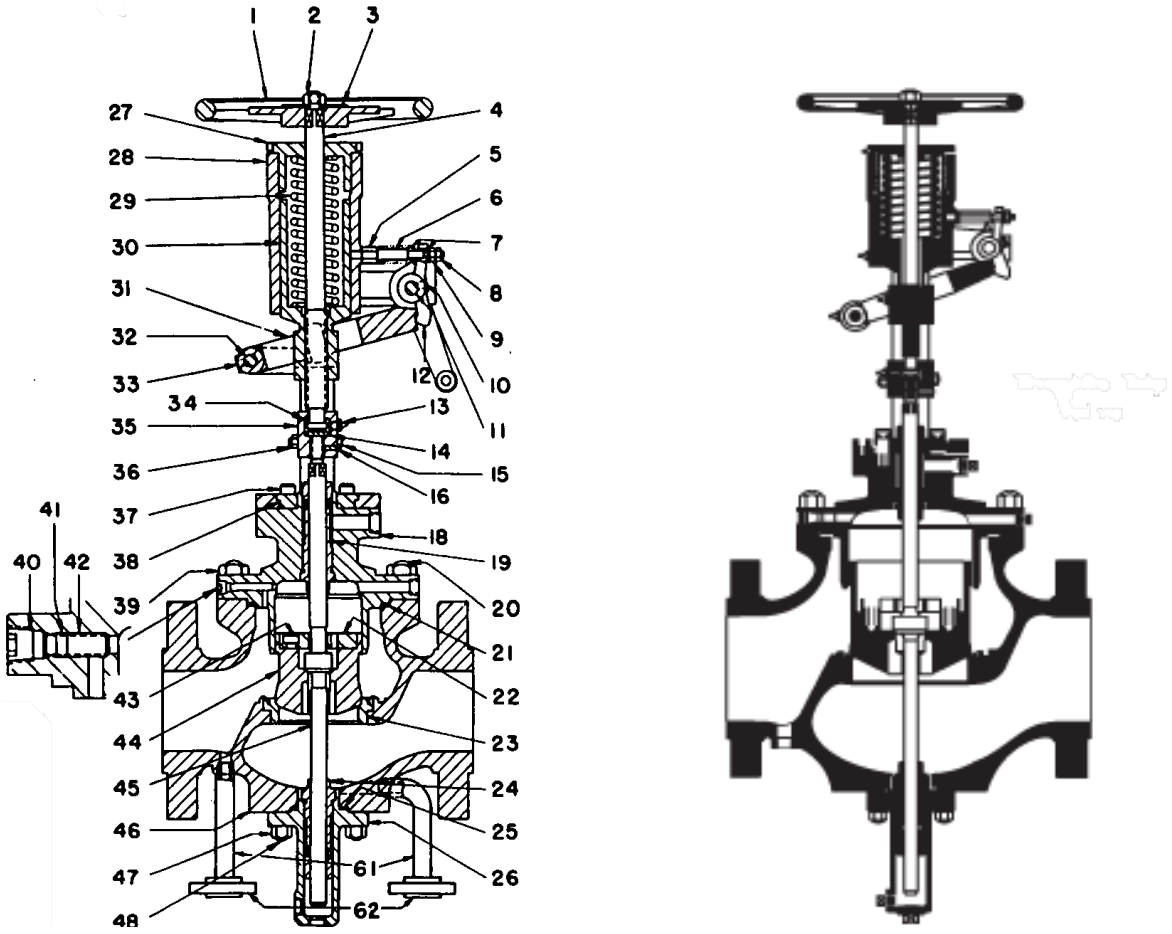

Figure 3: Trip-Throttle Valve Schematic. Reprinted from [5,6]

The GV is a Terry brand, single seated, pressure balanced 3” diameter cylindrical plug valve with a nominal 4” inlet [5]. An external governor controls the plug position via linkages on top of the valve. This regulates the process fluid flow to the turbine in order to achieve the desired rotational speed. Figure 4 shows a schematic of the GV.

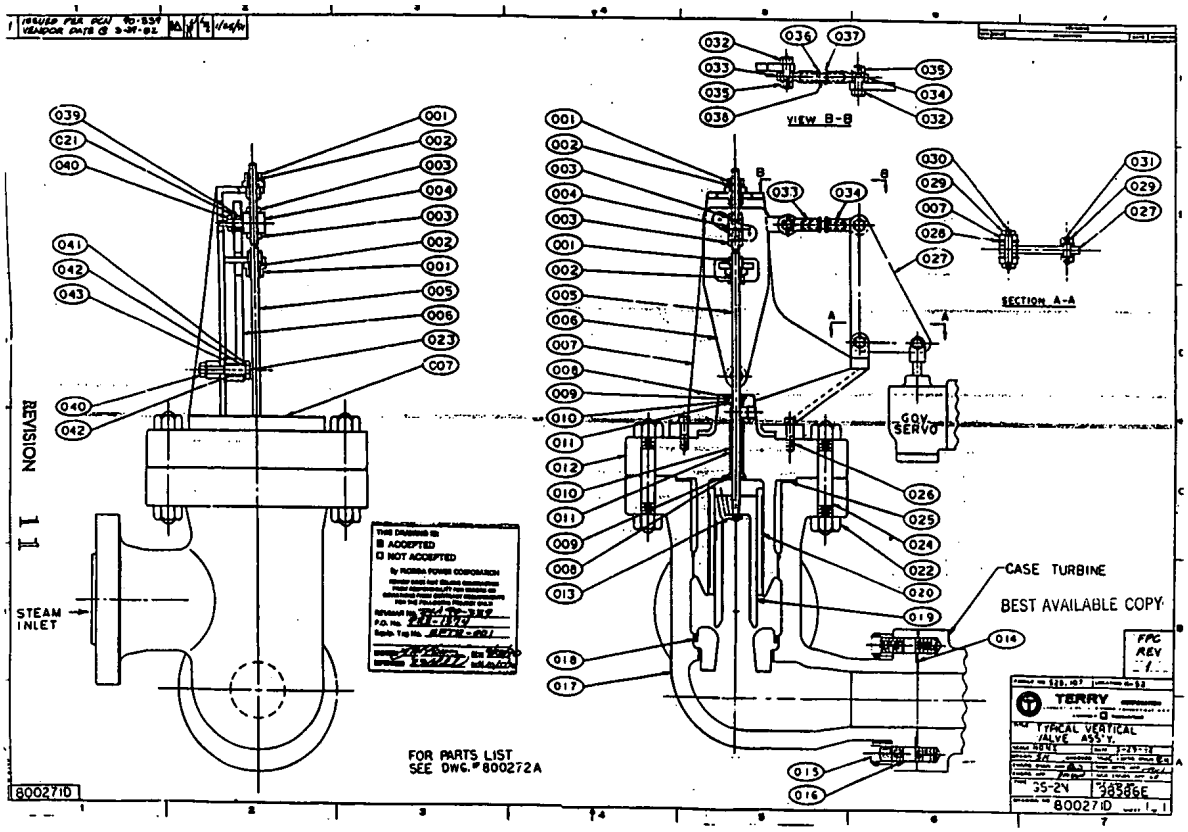

Figure 4: Governor Valve Schematic. Reprinted from [5]

Within the RCIC package, the steam lines are connected to the TTV. The GV sits immediately downstream of the TTV and is mounted to the turbine on the exit side. Figure 5 shows the flow path through the control valves upstream of the turbine.

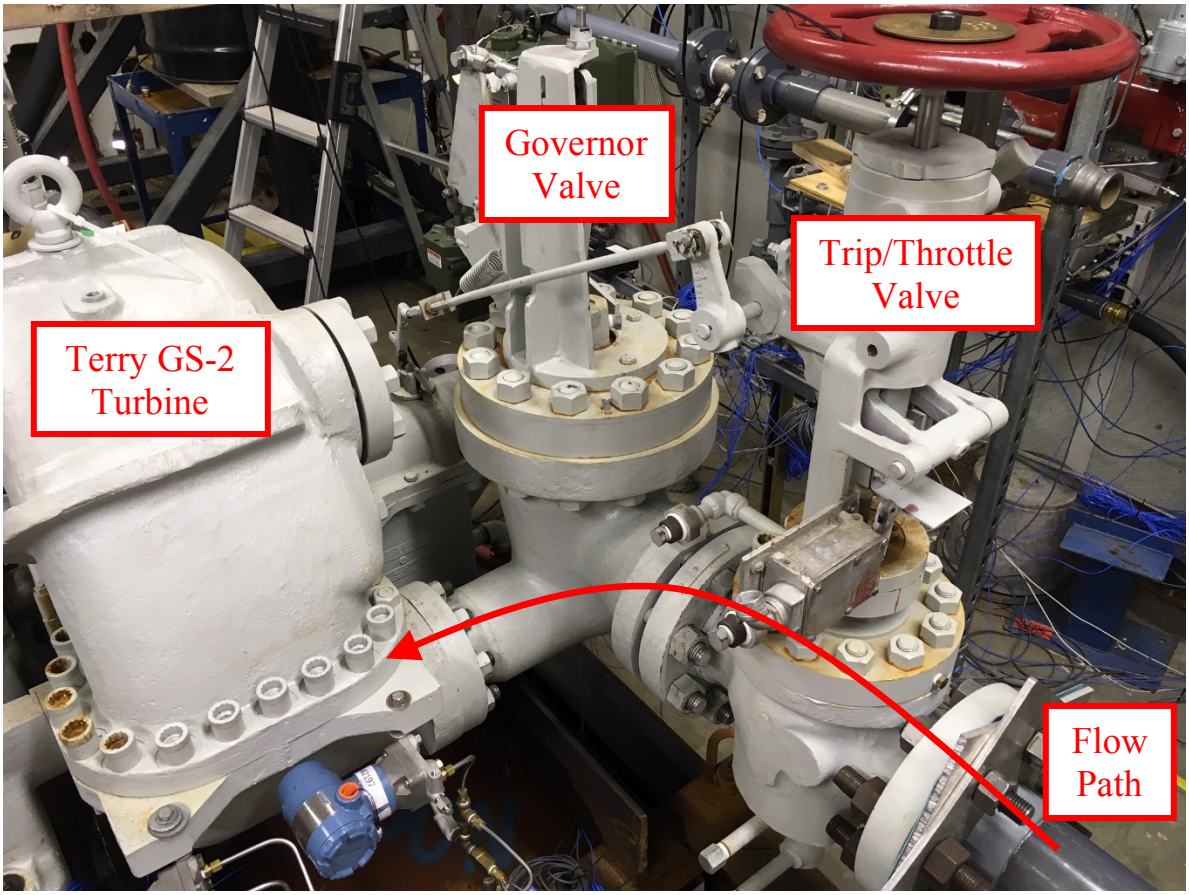

Figure 5: Process Fluid Flow Path Through Valves

1.3.1. Component Valve Testing

In order to best understand the RCIC system behavior under air/water conditions, the control valves were included in the test loop. However, for the purposes of validating computer simulations, each valve must be modeled independently so its effects can be subtracted out from the aggregate, leaving solely the effects of the Terry turbine.

A useful and widely accepted parameter for characterizing the effects of an individual valve is the flow coefficient, C_v. The flow coefficient is an empirically derived parameter which relates the flow rate through a valve (in GPM) to a 1 psi energy loss,

measured as a pressure drop. In practice, knowledge of the flow coefficient allows for determination of the flow rates and energy losses through process valves [7]. Flow coefficient is a function of valve geometry and stem withdrawal position, and can be determined either experimentally or through theoretical estimation. Frequently theoretical estimations do not account for various intricacies of internal geometry and may lead to poor results [8]. Although more resource intensive, experimental measurements provide a more accurate picture of the valve characteristics.

1.4. Present RCIC System Self-Regulating Mode Theory

Current hypotheses suggest the RCIC turbine was operating under two-phase (steam/water) flow during much of the 70+ hours, due to the presence of an abnormally high level of liquid water in the RPV. The water level was high enough to enter the main steam lines exiting the reactor, thus creating a two-phase mixture on the inlet side of the turbine. Due to the loss of control of the RCIC system through the governor valve and the extended 70-hour system operation, it is believed the turbine was running in a self-regulating mode during much of the accident. If the inlet flow to the turbine was largely steam, the turbine could extract more work and thus power the pump to provide more water to the reactor core. The additional water in the vessel core would cause the water level to reach the main steam line exit and enter the turbine inlet flow, decreasing the power output of the turbine and the water supplied by the pump.

2. LITERATURE REVIEW

Studies by the Terry Company [9] showed the turbine can withstand the injection of water slugs; however, little is known about turbine performance under continued liquid water injection and its ability to recover from such events. Therefore, characterization of the Terry turbine's behavior and performance curves under two-phase conditions is necessary for a better understanding of the RCIC system's potential to remove decay heat under emergency situations when regulation and control of the turbine is unavailable.

Before the Fukushima accident, the assumed operational envelope of the Terry turbine was mostly based upon the manufacturer's data. Operating limits and system models assumed ideal Terry turbine and pump performance. Under beyond design basis event (BDBE) conditions, RCIC system performance is not well understood. The events during the Fukushima accident prompted several research studies to better understand the operating envelope of the Terry turbine, especially under BDBE conditions.

Initial accident models were developed in a severe accident simulation code, SAMPSON, by Suzuki [10]. These simulations assumed a reduced power output from the RCIC turbine due to the presence of water, and torus room flooding. The simulation could reproduce physical parameters during the accident in the RPV and the primary containment vessel, and also predicted the eventual RPV failure; however, there were multiple remaining unknowns. Subsequent studies further investigated the RCIC system behavior and accident progression.

Lopez [11,12] modeled the RCIC system on unit 2 during the 70 hour self-regulating, two-phase flow window, under the assumption that the presence of water would reduce the power output of the RCIC turbine. Subsequently, a degradation coefficient, representing the turbine power reduction as a function of flow quality, was developed from the non-homogeneous equilibrium model for two-phase flow. When including the degradation coefficient in accident simulations, results aligned more closely with the accident investigators' findings and the data recorded from the actual accident. This model demonstrates the self-regulating phenomenon, indicating the RCIC system had some sort of internal feedback mechanism to control behavior without human intervention. Kim [1] found that the unit 2 accident progression is dependent upon the RCIC system's operating conditions. RCIC conditions affected fuel temperatures and the rate of fission product release into the environment. The effect of torus room flooding, due to the tsunami, was also shown to affect RCIC system performance. Li [13] performed a sensitivity analysis of the unit 2 accident and provides a possible accident progression. The effects of void fraction, suppression pool thermal stratification, and the introduction of seawater to the RCIC system by fire engines are considered. Fernandez [14] modeled the events in unit 3 during the accident. The unit 3 RCIC system ran for approximately 20 hours before it tripped, likely due to a high exhaust pressure signal. Pellegrini [15] modeled unit 3's accident progression from start to vessel failure. This analysis focused on cooling water levels and flow rates and considered the effects of multiple different cooling systems, including RCIC, throughout the accident. Zhou [16] developed a series of analytical models characterizing the turbine nozzles. The models predict a two-part expansion process for the steam: first, adiabatic

expansion across the turbine nozzle, and second, free-expansion after exiting the nozzle. The two-part model can predict steam flow rates and velocities, both of which are necessary for accurate turbine modeling; however, these models are unable to incorporate two-phase flow scenarios. An aim of this work is to provide experimental data for a two-phase flow, nozzle expansion model.

Multiple previous studies have aimed to characterize two-phase flow regimes. Baker [17] was the first to publish a two-phase flow characterization map. His map, along with maps by Spedding and Nguyen [18], and Hewitt and Roberts [19], are some of the commonly used maps for classifying two-phase flows. Generally, these maps do not incorporate the effect of elevated pressures on flow regime. Some studies have aimed to classify two-phase flows through microchannels [20,21], and some have studied the interfacial area between the phases [22,23]. However, there is not much data available in the literature characterizing two-phase flow regimes at elevated pressures.

Previous research at Texas A&M, by Luthman [24], led to the development of experimental methods for characterizing Terry turbine performance given a two-phase inlet flow. A Terry ZS-1 turbine was tested under both air/water and steam/water conditions over a range of inlet qualities (gas mass fraction) and turbine rotational speeds. Patil [25,26] conducted further testing on a Terry ZS-1 turbine under air/water two-phase inlet conditions. The results indicated torque decreased with increasing shaft speed, or with decreasing air mass fraction (increasing water content), or with decreasing inlet pressure while holding the other parameters constant. Efficiency appeared to peak over the rotational speed range, but decreased with decreasing inlet pressure or decreasing air mass fraction (increasing water

content). The efficiency appeared to rise again at extremely low air mass fractions (below 10%); however, this was likely due to the inaccuracy of the isentropic assumption at low air mass fractions. At low air mass fractions, an isothermal assumption was suggested instead to improve agreement between experimental data and expected results. These results agreed with the preliminary testing done by Luthman [24].

3. OBJECTIVES

The disaster at Fukushima demonstrated that the RCIC system has a larger operating envelope and a greater ability to dissipate decay heat than previously expected. The project sponsors want to have a better understanding of the RCIC system's performance and potential for use as a failure mitigation system. The project's findings may help engineers to implement safety related design and operational changes in new and existing facilities alike.

The overall objective of this work was to develop an experimental database for validating computer simulation models of the Fukushima accident. Sandia National Laboratories and Idaho National Laboratories are leading efforts to model the overall accident, as well as key subsystems, such as the RCIC system. Sandia National Laboratories is using their internally developed MELCOR simulation code, while Idaho National Laboratories is using the RELAP simulation code.

This work had several experimental objectives. The first was to characterize the TTV and GV through individual component testing to experimentally determine the flow coefficient, C_v, at a variety of valve positions. An accurate understanding of the flow coefficient is important for understanding and predicting how the TTV and GV affect the incoming flow to the turbine.

The larger, second objective was to demonstrate the Terry turbine's ability to withstand repeated water injection and to develop performance curves under two-phase (air/water) inlet conditions. The turbine was tested under numerous operating conditions with the inlet pressure of the turbine, the quality (or air mass fraction) of the incoming flow

and the rotational speed of the turbine varied with each test. This information allows for a better understanding of the decay heat removal potential of the RCIC system and quantifies the performance degradation of the Terry turbine under two-phase flow.

A third objective was to understand the interaction between the gaseous and liquid phases of the two-phase flow, especially at elevated pressures within the turbine nozzles. A flow visualization section was installed adjacent to the trip throttle valve and governor valve mounted to the turbine. A high-speed camera recorded the two-phase flow, which changed with pressure and quality, as it entered the turbine skid.

This work was a continuation of the work performed by Patil [25]. Instead of using the small scale ZS-1 turbine, a full-scale GS-2 turbine was used for this study. The data was collected using the same techniques and similar equipment as the data from the Terry ZS-1 turbine.

4. EXPERIMENTAL FACILITIES

A multiphase test loop was constructed for testing the individual valves (denoted valves) and the Terry turbine skid (denoted turbine). The test loop was modified and adapted as necessary to meet the required specifications for a given test. The flow loop utilizes air, water and mixed process lines. Air is supplied to the air process lines via oil-free, screw compressors. These compressors have a total capacity of 2500 cfm at 120 psig. Inline air filters maintain the air supply cleanliness and humidity. There are two air supply lines connected to the valve or turbine entrance due to the large volume of air necessary to test the given specimen. The first air supply line has three parallel flowmeter lines and the volumetric flow rate determines which flow meter is used for best accuracy. The second air supply line has a single flowmeter, and is used to supplement the first air supply line when higher volumetric air flow is needed.

Outside, a 5000-gallon water tank is filled with city water, which is connected to a centrifugal pump to boost process water pressure and a water filter to help clean the loop water. As with the first air supply line, the water line splits into multiple parallel metering lines to measure the flow rate. The test's required flow rate determines which of the four meters is used, depending on the specific flow meter capacities.

After flow measurement, both air process lines and the water process line combine to create a multiphase flow line, which enters either the valve or the turbine, depending on the test. Upon exiting the valve or turbine, the multiphase process fluid returns to the outdoor tank. The air vents to atmosphere while the water is recirculated within the flow loop.

4.1. Valve Test Rig Components

The test loop was set up to accommodate testing of the flow coefficient of the TTV and the GV according to the International Electrotechnical Commission (IEC) 60534-2-3:2015 standard [27]. Figure 6 shows a schematic of the valve flow coefficient test loop. In order to ensure a well-developed flow pattern at the entrance to the valve, the IEC standard specifies an entry length of 20 times the nominal diameter (20 D). Similarly, to ensure the downstream flow does not affect the fluid flow exiting the valve, a 7 D exit length is specified. To measure the energy losses across the valve, pressure taps are placed at 2 D upstream of the valve, and 6 D downstream of the valve. A longer downstream pressure tap location is required to allow the velocity profile to re-normalize after the valve, so as to capture both static and dynamic pressure losses through the valve [7]. These lengths are depicted graphically in the schematic. Pictures of the TTV and GV installed in the test loop are shown in Figure 7 and Figure 8, respectively.

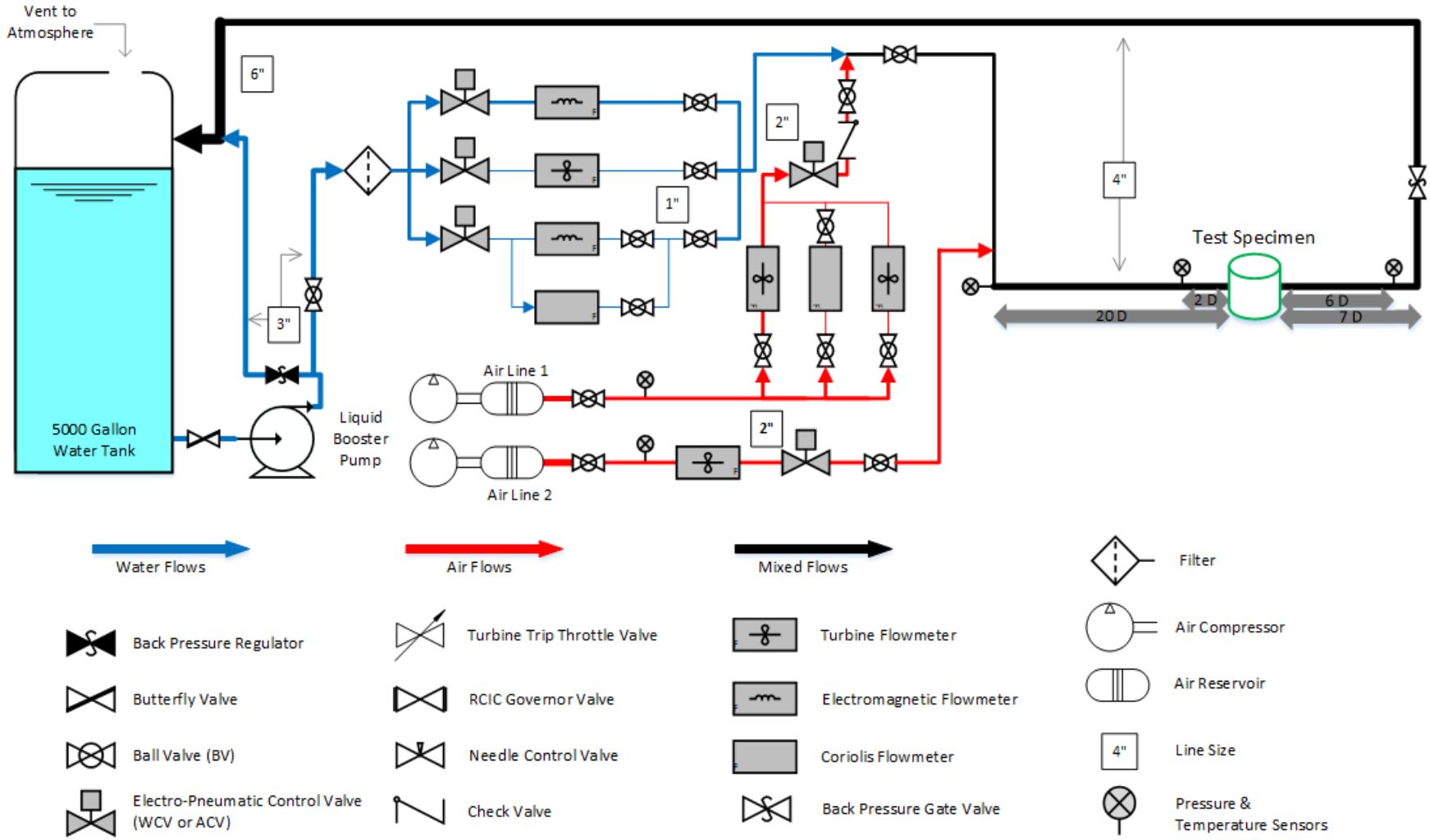

Figure 6: Valve Test Loop Schematic

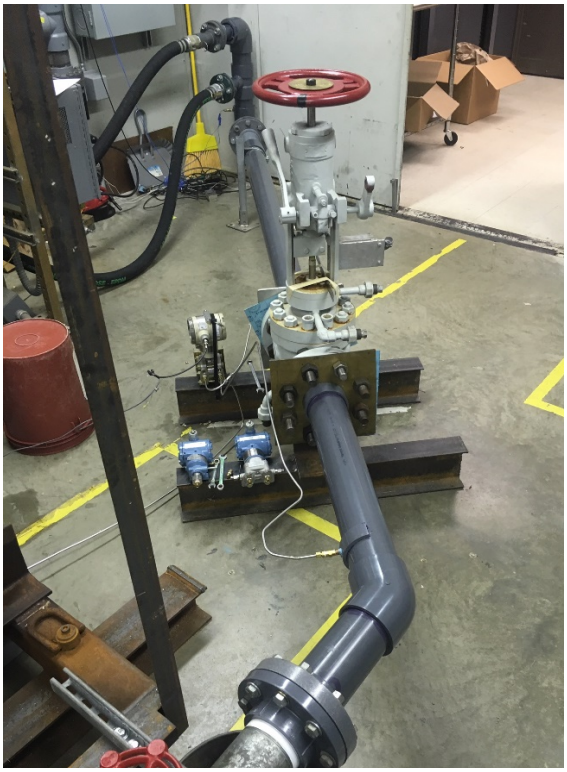

Figure 7: TTV Flow Coefficient Test Setup

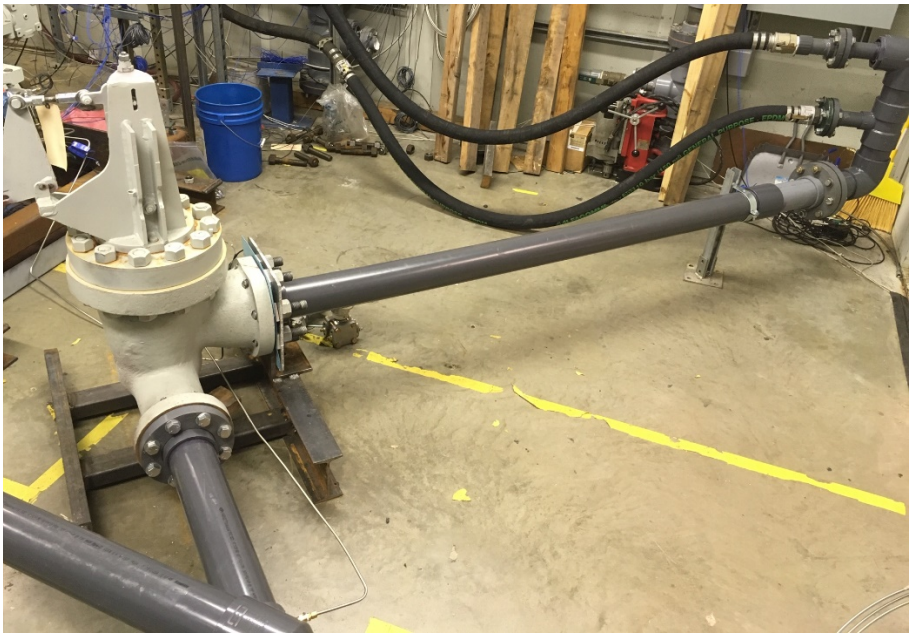

Figure 8: GV Flow Coefficient Test Setup

4.2. Turbine Test Rig Components

Figure 9 shows a schematic of the turbine performance test loop. After the air and water process lines combine to create a multiphase flow line, there is a 32-inch (8 D) entry length to the turbine and attached valves in order to homogenize the flow. To better understand the effects of two-phase flow, especially within the turbine nozzles, a flow visualization section is installed within the entry length, adjacent to the attached valves.

A water brake dynamometer directly coupled to the turbine output shaft loads the shaft, and varies the angular velocity. A load cell, connected between the dynamometer arm and a fixed support, measures the turbine torque. A thermocouple, epoxied to the front bearing housing, measures the external housing temperature. This data shows the heat buildup over time and the effect of water slug injection on bearing housing temperature. Figure 10 highlights the locations of the water break dynamometer, load cell, and bearing housing thermocouple on the turbine skid. Figure 11 and Figure 12 show the inlet and outlet sides of the turbine and the connected piping.

.

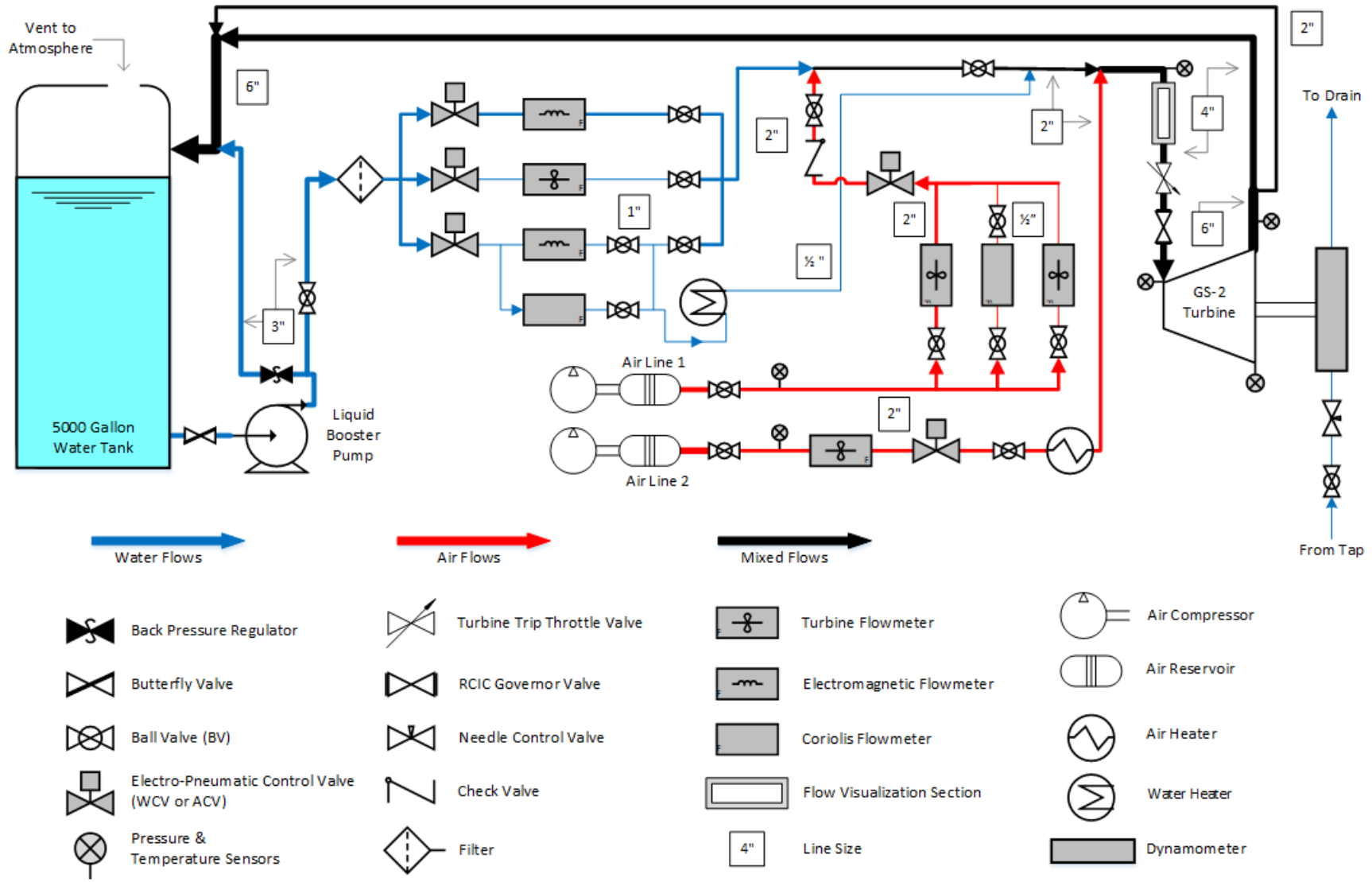

Figure 9: Turbine Test Loop Schematic

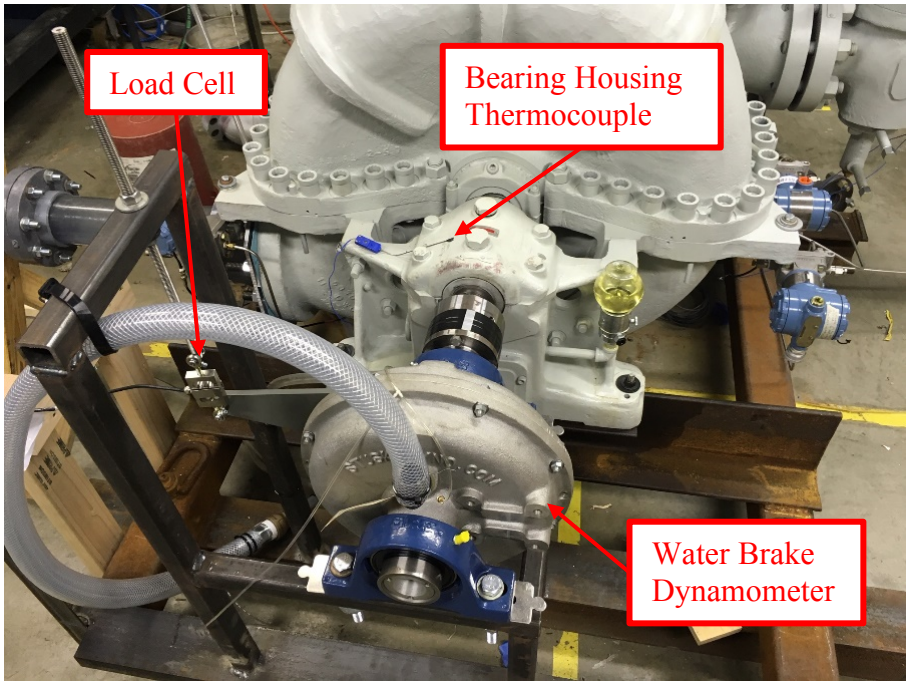

Figure 10: Turbine Test Rig with Detailed Location of Water-Brake Dynamometer, Load Cell, and Bearing Housing Thermocouple

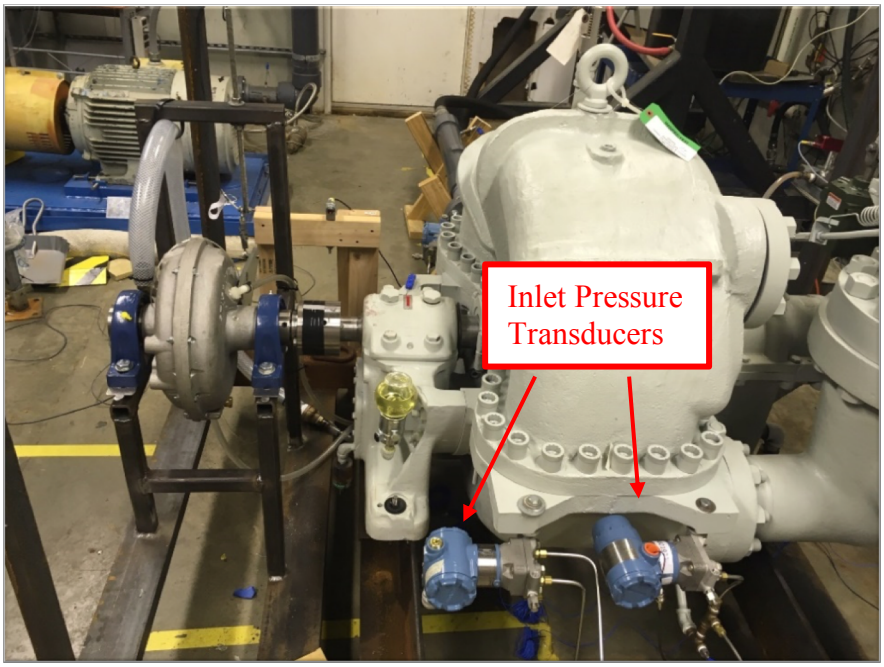

Figure 11: Turbine Test Rig with Detailed Location of Inlet Pressure Transducers while Looking at Inlet Side

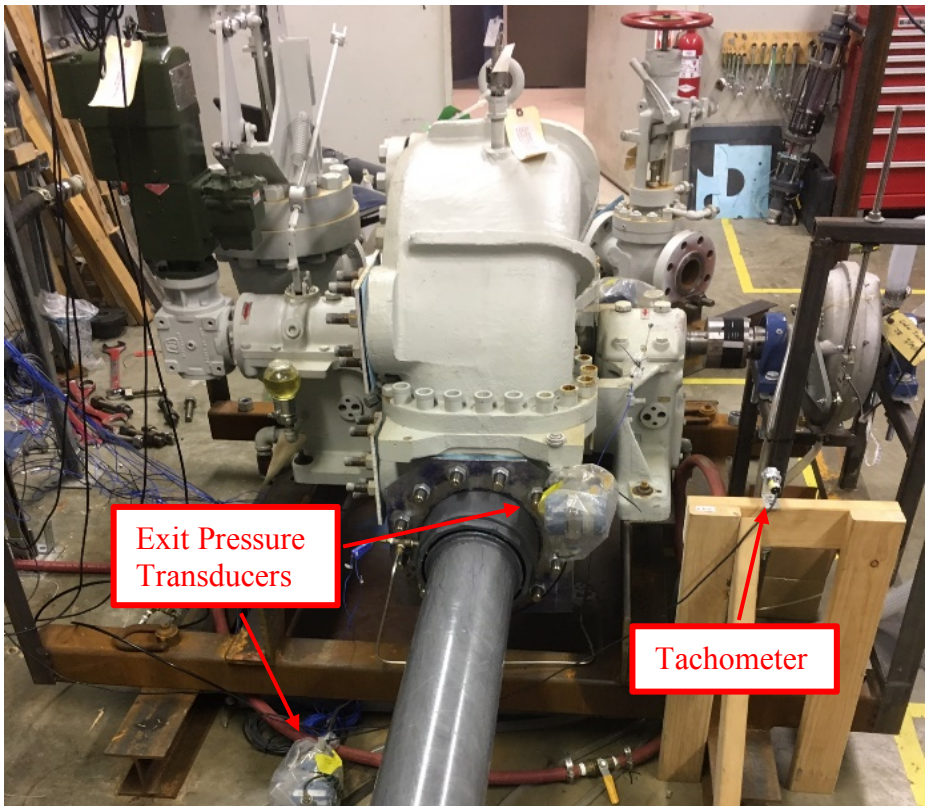

Figure 12: Turbine Test Rig with Detailed Location of Exit Pressure Transducers while Looking at Outlet Side

During testing on the small-scale Terry ZS-1 turbine, Patil [25] observed sub-freezing temperatures (of water) at the turbine exit when testing with single-phase air, due to the significant expansion of air across the turbine. The MELCOR accident simulation code being developed by Sandia National Laboratories does not predict system behavior well near or below the freezing point of water. Since these experimental results will be used for validation of the MELCOR code, the temperatures on the discharge side of the turbine needed to be raised. To do so, an inline air heater was added to preheat the incoming air stream. Similarly, in this work, an inline air heater was connected to the second, larger capacity, air supply line to preheat the process air.

Similar to the inline air heater in the air process lines, an inline water heater is connected to the smaller liquid metering lines. This tank-less water heater is included because of the possibility of sub-freezing discharge temperatures when testing high air mass fraction, multi-phase process flows.

5. ANALYSIS METHODS

5.1. Valve Analysis

Evaluation of the valves followed the IEC 60534-2-3:2015 standard [27], which outlines the testing and evaluation procedures for flow capacity in industrial process control valves. Both valves were tested with both incompressible (water), and compressible (air) mediums. When using water as the process fluid, the IEC standard calculates the flow coefficient as

$$C_v = \frac{Q_g}{0.0865}\sqrt{\frac{\rho/\rho_0}{\Delta p}} \tag{1}$$

with Q_g as the gas flow rate in $\frac{m^3}{hr}$, $\rho/\rho_0 = 1$ for water at 15 °C (59 °F), and Δp as the pressure differential across the test specimen in kPa. Testing of the valve should be done at various back pressures (pressure drops). The flow coefficient is calculated at each of the back pressures, and the average value is taken as the flow coefficient for the given valve and position.

Alternatively, when using air as the process fluid, the compressibility of air must be considered. The flow coefficient equation is modified using an expansion factor, Y.

$$YC = \frac{Q_l}{22.5\ p_1}\sqrt{\frac{MT_1}{x}} \tag{2}$$

In equation $YC = \frac{Q_l}{22.5\ p_1}\sqrt{\frac{MT_1}{x}}$(2), Q_l is the liquid flow rate in $\frac{m^3}{hr}$, p_1, is the absolute pressure upstream of the test specimen in kPa, M, is the molar mass of the compressible

process fluid in $\frac{kg}{kmol}$, T_1, is the upstream absolute temperature of the process fluid in K, and x is the dimensionless pressure ratio, defined as

$$x = \frac{\Delta p}{p_1} \tag{3}$$

with both parameters the same as previously defined. Data is recorded at various pressure drops (with a constant upstream pressure) to vary dimensionless pressure ratios. The results are plotted on linear coordinates as YC *vs.* x, with a linear trendline applied to the data. The trendline is extrapolated to the y-axis where $Y = 1$ when $x = 0$. This intersection is denoted $(YC)_0$ and is the value for C_v for the given valve and position. Additionally, the x_T value is taken from the curve as the pressure differential ratio at $(YC) = \frac{2}{3}(YC)_0$. The x_T value is the pressure differential ratio factor for a valve for choked flow.

5.2. Turbine Analysis

An energy balance was employed to evaluate the work transmitted out of the Terry turbine shaft. The power input into the turbine has two separate components: one from the gas, and one from the liquid. The gas input power is modeled using isentropic expansion equations, while the liquid input power is modeled using isothermal, steady flow equations for incompressible substances. The turbine isentropic efficiency is given by,

$$\eta_{isentropic} = \frac{Power_{output}}{Power_{Input}} = \frac{\dot{W}_{shaft}}{P_{gas}+P_{liquid}}. \tag{4}$$

The shaft power, given below, is a function of torque, τ, and rotational speed, ω.

$$\dot{W}_{shaft} = \tau\omega \tag{5}$$

The torque, τ, is calculated from the dynamometer arm length and force reading from the attached load cell. The gas input power is a function of a polytropic constant, n, the turbine inlet pressure, p_{inlet} turbine inlet volume flow rate, $\dot{V}_{inlet}$, and turbine outlet pressure, p_{outlet}. For isentropic expansion, the polytropic constant, n, is the specific heat ratio (1.4 for air).

$$P_{gas} = \frac{n}{(1-n)} p_{inlet} \dot{V}_{inlet} \left[\left(\frac{p_{outlet}}{p_{inlet}} \right)^{\frac{n-1}{n}} - 1 \right] \quad (6)$$

The pressure values are measured directly, while the inlet gas volume flowrate is calculated from the ideal gas equation. At the upstream gas flow meter, the gas pressure, p_{FM}, temperature, T_{FM}, volume flowrate, $\dot{V}_{\mathrm{FM}}$, and gas constant, R, are known. Using the ideal gas equation of state,

$$p\dot{V} = \dot{m}RT, \quad (7)$$

the gas mass flow rate, $\dot{m}_{gas}$, is calculated. As mass is conserved, the gas mass flowrate is the same at the turbine inlet, as at the flowmeter. With the measured temperature and pressure at the turbine inlet, the ideal gas equation can be used again, to calculate the turbine inlet volume flowrate $\dot{V}_{\mathrm{inlet}}$. Lastly, the liquid input power is a function of the liquid flow rate, Q_l, and the pressure drop across the turbine, $(p_{inlet} - p_{outlet})$, which are all measured directly.

$$P_{liquid} = Q_l \cdot (p_{inlet} - p_{outlet}) \quad (8)$$

6. OPERATING PROCEDURES

6.1. Valve Procedures

Both the TTV and GV were tested at multiple positions throughout their respective range for experimental determination of C_v. The TTV had a total stem withdrawal of 1.73", which corresponded with approximately 9.0 revolutions of the valve's hand wheel, while the GV had a total stem withdrawal of 0.68", which corresponded with approximately 8.5 revolutions of the positioning nut. As the GV does not have a mechanism for manually setting the stem position, a ½"-13 hex nut was threaded onto the valve stem in order to manually vary the stem height during testing as shown in Figure 13. The black marks on the nut and valve were used as indicators for determining the nut/stem position.

Figure 13: Governor Valve Linkages with Attached Stem Positioning Nut and Positioning Nut Indicators

The TTV was tested for leaks at the fully closed position (0 revolutions) and at the contact point (approx. 0.25 revolutions), where the internal plug mechanism is initially at contact with the valve seat without a pre-loaded force. Flow coefficient tests were executed at every half hand wheel revolution of stem position from 1 revolution to 4 revolutions open. Between 4 and 9 revolutions open, C_v tests were executed at every whole revolution. The GV was tested in a similar manner. Leak tests were done at the fully closed position (0 revolutions). Flow coefficient tests were run at every quarter revolution between 0 and 1 revolutions, at every half revolution between 1 and 4 revolutions, and every whole revolution between 4 and the fully open position (~8.5 revolutions).

Separate procedures were used for testing the flow coefficient with air and with water. For air testing, the "alternate method" according to the IEC standard was used. As with the single-phase turbine tests, the air inlet is regulated by two electro-pneumatic control valves. A large pressure drop is desirable in order to choke the air flow and achieve the maximum mass flow rate through the valve for the given stem position. At lower (more closed) valve positions, the air flow through the valve was choked with an upstream pressure of at least 50 psia and atmospheric downstream pressure. To check if the process air is choked, the pressure drop across the valve is reduced to 90% of the previous value. If the new flow rate is within 2% of the original flowrate, the first point is considered choked. After the TTV and GV were more than 3 revolutions open, the flow could no longer be choked due to the capacity limitations of the facility. For each valve stem position, the back pressure was gradually increased by closing a downstream throttling valve. Steady-state

process parameters were recorded at 4 or more conditions between the maximum achievable flow rate and zero flow (zero pressure differential).

Flow coefficient tests with water followed a similar procedure. While testing at low valve stem positions, the process fluid was choked through the valve in order to achieve the maximum mass flow rate for the given stem position. After the valve was 1.5 stem revolutions open, the flow was no longer choked through the valve due to the limitations of the facility. As with air, for each stem position, the back pressure was gradually increased by closing a downstream throttling valve. The process parameters were recorded at steady state for 3 or more conditions between the maximum achievable flow and zero flow for the given test valve position. For each condition, the flow coefficient is calculated, and the average value is taken as the flow coefficient for the given test valve position. The main notable difference between the water and air tests was that the water flow was choked in the upstream metering lines after the valve stem was 3 revolutions (~ 1/3) open. Due to the facility limitations, the TTV and GV were not tested at higher (larger flow area) stem positions with water as the process fluid.

6.2. Turbine Procedures

6.2.1. Test Ranges

The turbine is operated at inlet pressures ranging from 20 psia (1.38 bar) to 70 psia (4.83 bar) with the air mass fraction at the turbine inlet varying from 5% to 100%. Dynamometer loading controls the shaft speed, which varies from ~300 RPM to ~3600 RPM. Table 1 summarizes these process parameters and gives values that were used during

testing. These variables are commonly used to characterize rotating equipment such as pumps, turbines, and compressors.

Table 1: Testing Variables and Values

Parameter	Values	Units
Inlet Pressure	20 (1.38), 30 (2.07), 50 (3.45), 70 (4.83)	psia (bar)
Flow Quality	100, 95, 90, 80, 70, 60, 50, 40, 30, 20, 10, 5	%
Rotational Speed	~300 to ~3600 (multiple points)	RPM

6.2.2. Single Phase Tests

For single-phase tests, the turbine inlet flow is 100% air, with a relative humidity of about 20%. The air inlet pressure is controlled by using two electro-pneumatic control valves as explained in the operating procedure. The turbine is initially loaded by supplying water to the dynamometer. Air is gradually introduced until the inlet pressure reaches the desired levels. The dynamometer is loaded to control the turbine shaft speed. Water flow to the dynamometer is regulated via an electrically controlled needle valve. The air inlet pressure and flow quality are specified prior to testing. Rotational speeds are not specified prior to testing, as it is extremely difficult to control the turbine to within ±20 RPM of a given target. Steady state data is recorded at multiple speeds within the operating envelope of the turbine. To shut down after testing, the air supply is first closed, then the dynamometer is drained and turbine unloaded after the turbine has come to a stop.

As previously mentioned in the EXPERIMENTAL FACILITIES section, while running the small-scale ZS-1 turbine, exit temperatures of the single-phase air flows were

below the freezing point of water. Shakedown testing on the GS-2 turbine showed a similar behavior at 50 and 70 psia inlet pressures. Since this experimental data will be used to validate the MELCOR simulation codes, the inline air heater is utilized to preheat the incoming air flow in order to help boost exit temperatures.

6.2.3. Multiphase Tests

Procedures for the multiphase tests are identical to the single-phase tests except for the addition of water to the process flow. Water is supplied to the dynamometer to load the turbine, and the external booster pump is started to pressurize the water supply line. The air supply line(s) are opened, using two electro-pneumatic control valves, until the desired inlet turbine pressure is achieved. Next, the appropriate water control valve is opened, depending on the necessary flow rate to achieve the specified inlet air mass fractions. Subsequent adjustments to the air and water supply control valves may be necessary to reach the desired inlet pressure. The dynamometer loading is changed to obtain various rotational speeds. As with the single-phase tests, rotational speeds are not specified prior to testing.

During testing, steady state data is recorded at the specified conditions. To shut down after testing, the water supply valve is first closed, then the air valve(s). The dynamometer control valve is closed after the turbine has come to a stop.

7. TWO-PHASE FLOW ANALYSIS

Gas volume fraction (GVF) and gas mass fraction (quality) are two different ways of quantifying two-phase flow. As their names imply, GVF describes the amount of gas in the flow by volume while gas mass fraction describes the amount of gas in the flow by mass. The significant difference between gas and liquid densities frequently causes a multi-order relationship between GVF and gas mass fraction. Generally, GVF is more sensitive to the addition of gas to mostly liquid flows, while gas mass fraction is more sensitive to the addition of liquid to mostly gaseous flows. As the incident at Fukushima involved the addition of liquid (water) to primarily gaseous (steam) flows, gas mass fraction is used to quantify the two-phase flows in this work.

7.1. Flow Visualization

A flow visualization section was installed immediately upstream of the TTV to characterize the flow as it entered the turbine skid. Directly upstream, there was a 6-diameter entry section in order to establish a well-mixed flow entering the turbine. A Phantom V711 high-speed camera was used to capture and record images of the two-phase flow. The camera was set to record at 400 frames per second (fps). A backlit board was utilized to help distinguish between the air (white/light grey) and water (dark grey) phases. Figure 14 shows both the high-speed camera and the backlit board. Figure 15 shows images of the two-phase flow over the range of air mass fractions tested and for three inlet pressures ranging from 30 to 70 psia.

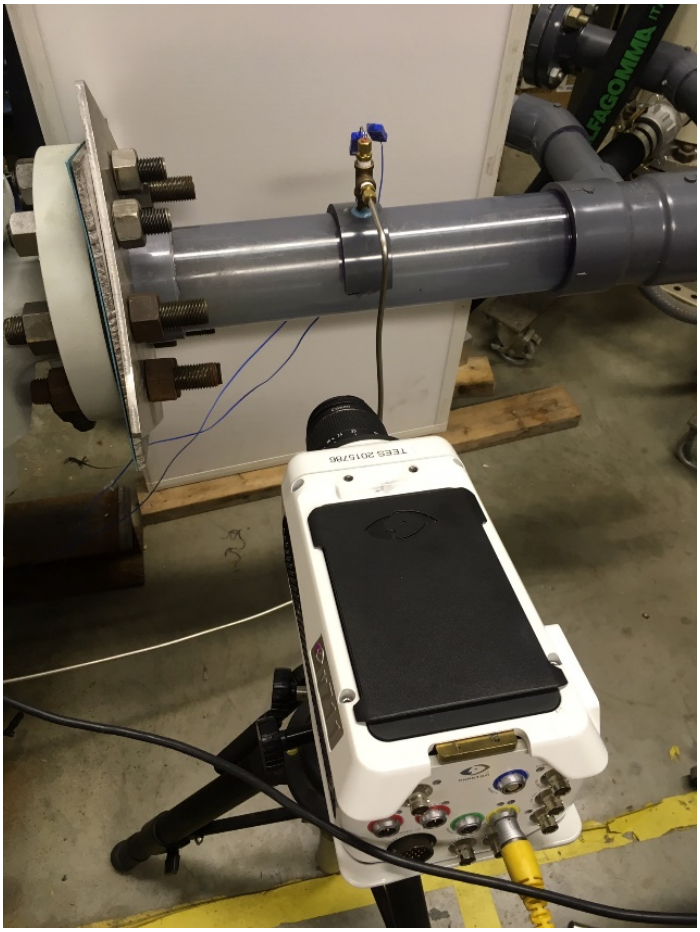

Figure 14: High Speed Camera and Backlit Board

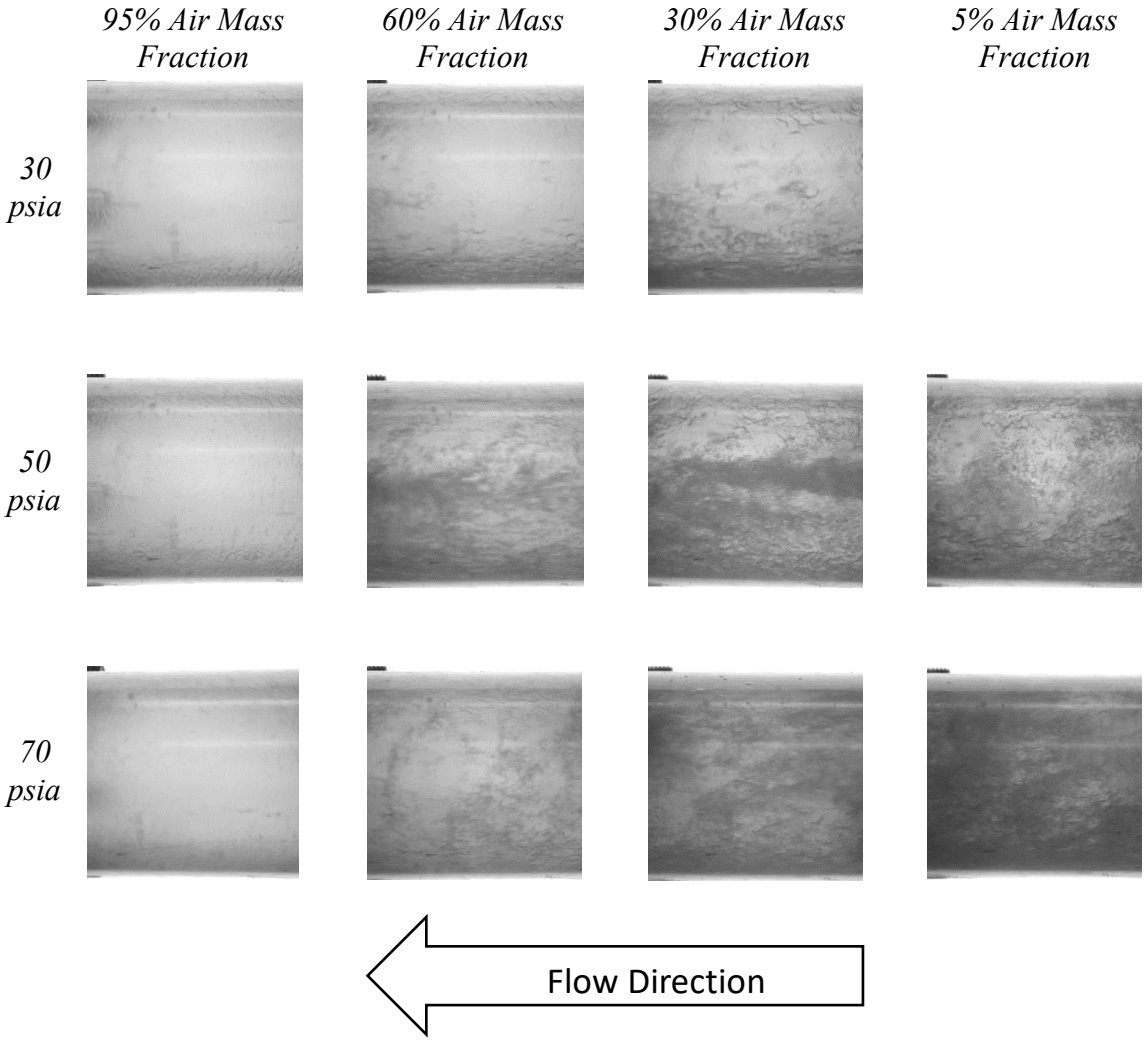

Figure 15: Flow Visualization at Various Air Mass Fractions and Pressures

7.2. Comparison with Existing Two-Phase Flow Maps

Before visual analysis of the flow regimes, a quantitative analysis was attempted for the flows displayed in Figure 15. Two different horizontal two-phase flow maps were used to classify the flow regimes based upon process parameters and flow medium properties. The Baker [17] map, shown in Figure 16, classifies the flow based upon mass flux and scaling parameters based upon density, surface tension and viscosity. At both the high (70

psia) and low (30 psia) range of pressures tested, all of the flows fell within the "Bubbly or Froth" section, as Figure 16 highlights. Characteristics of bubbly or froth flow include flows that are mostly liquid, but contain some gaseous phases as bubbles along the upper portion of the flow. This description clearly does not align with observations taken from the flow visualization pictures.

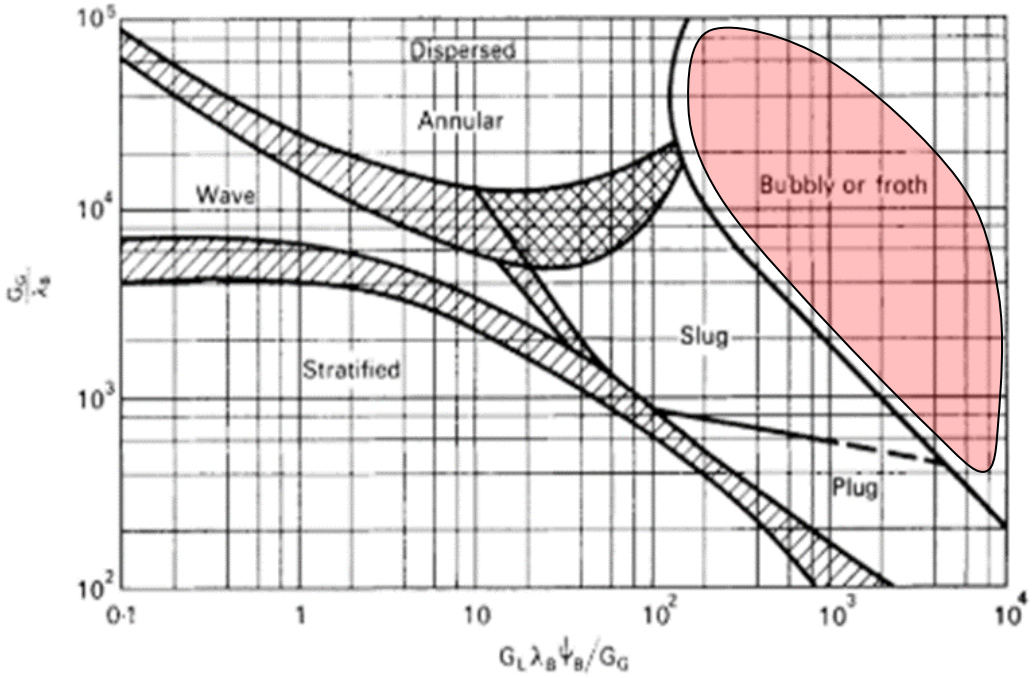

Figure 16: Baker Horizontal Two-Phase Flow Map

The Spedding and Nguyen [18] two-phase flow map, shown in Figure 17, characterizes the flow based upon the volumetric flow rate ratio and the square root of the Froude number. The Froude number relates the inertial forces to the weight of a fluid. At both 30 and 70 psia flows, the flows fell within the "Stratified" or "Stratified + Ripple" flow regimes. Flows at 70 psia and 5% air mass fraction fall along the "Slug/Stratified + Ripple"

border. Stratified flow is characterized by a clear vertical division within the pipe with the liquid on the bottom and the gaseous phase on top (i.e. the two phases do not mix). Stratified with ripple flow maintains the vertical division, but the interface between the two phases has ripples along the liquid surface due to shear stresses from the average velocity difference between the phases. As with the Baker map, these descriptions clearly do not align with the visual observations from the photographs.

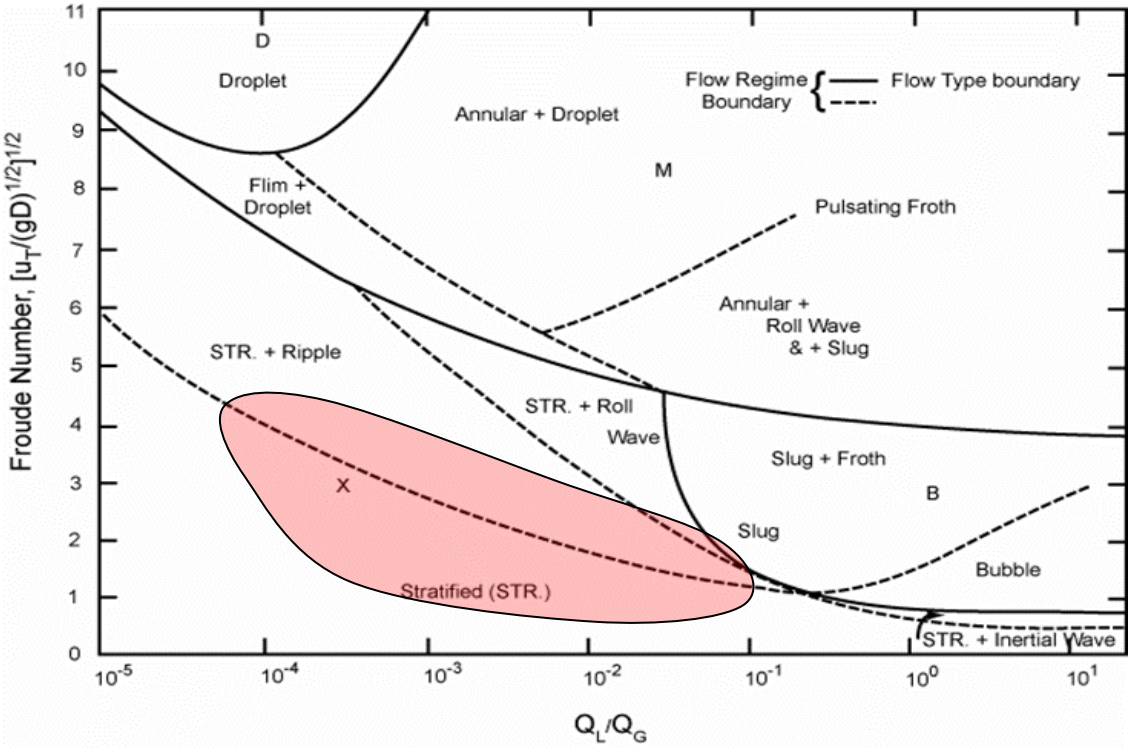

Figure 17: Spedding-Nguyen Two-Phase Flow Map

Neither of the horizontal two-phase flow maps accurately predict the flow regime. The disagreement between the maps and the images from this work is likely due to pressure differences. Both maps were developed for flows near atmospheric pressure. The flows

analyzed in this study operate at 2 - 4.5 times atmospheric pressure. The elevated pressures in a given cross-section increase the flow velocity and reduce the effect of body forces on the flow; thus, there is less vertical stratification. Further analysis was done using vertical two-phase flow maps as body forces are not considered.

The Hewitt and Roberts map [19] is widely cited for classifying vertical two-phase flow regimes. This map classifies flows based upon phase density and superficial velocity as shown in Figure 18. For high air mass fractions at 30 psia, the flows fell below the minimum range of the plot. If the plot were to be extrapolated, all of the flows would likely fall within the annular region. The flows at 5% air mass fraction fall near the annular-churn boundary. Overall, this prediction is much more adequate than those given by the horizontal flow maps, but inconsistencies still exist. The elevated pressure appears to shift the annular-churn transition to higher superficial velocities than predicted by the Hewitt-Roberts map. Additionally, the combination of multiple process fluid lines into the single entry section in the flow loop may contribute to instabilities that promote a churned regime at lower air fractions.

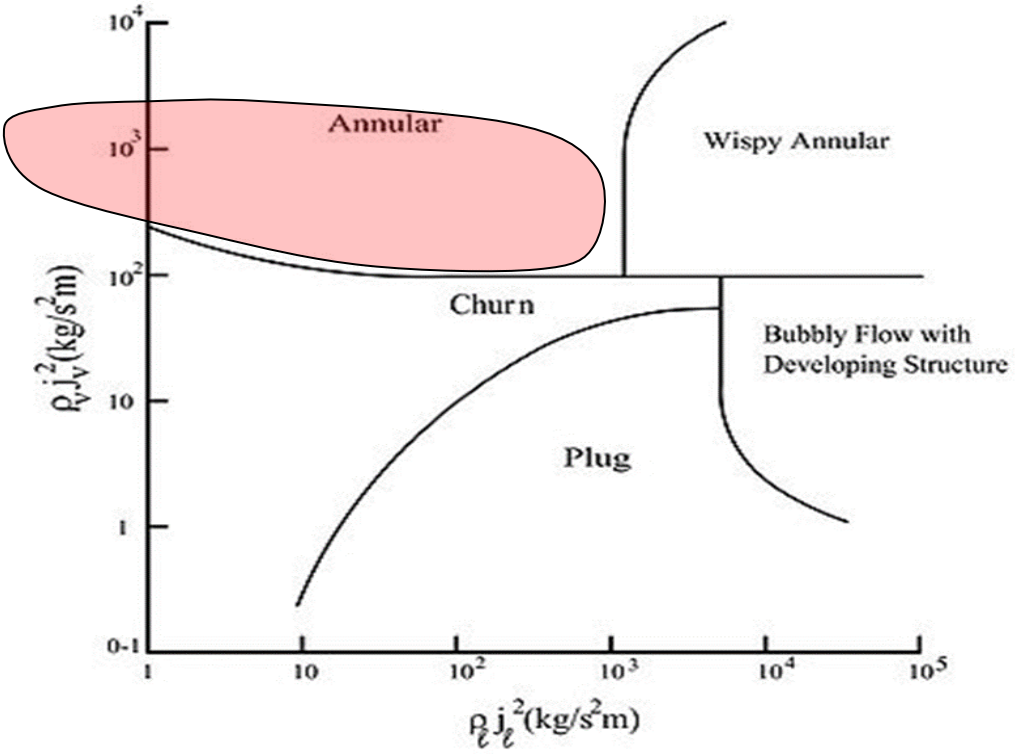

Figure 18: Hewitt-Roberts Vertical Two-Phase Flow Map

Generally, the two-phase flow maps do not predict flow regime well outside of the conditions for which they are prepared. Nevertheless, the vertical map was more accurate than the horizontal maps due to the diminished effect of body forces. Within horizontal flows, the elevated pressures cause better flow homogenization and a shift in flow regime as compared to two-phase flows at atmospheric pressure.

7.3. Visual Analysis

Visual inspection allowed for identification of various two-phase flow regimes within the range of air mass fractions tested in this experimental work. Churn and annular flow regimes are seen most often, with some mist flows as well. Slug and bubble flow

regimes are not seen as they typically occur in low GVF flows. As the lowest air mass fraction covered in this experimental work is 5%, the GVF for any trial was never below 90%; therefore, no slug or bubble flow regimes were encountered.

The first row in Figure 15 shows images of the two-phase flow entering the turbine over the range of air mass fractions tested at 30 psia inlet pressures. At high air mass fractions (top row, left image), the flow is in the annular regime with the majority of the water adhered to the pipe wall. The water layer appears fairly uniform with some ripples visible. Differences in fluid density and viscosity contribute to the significant segregation between the phases. At 60% air mass fraction (top row, left-middle image), the majority of the water still appears to be adhered to the pipe wall; however, the water layer is thicker, with a higher spatial density of ripples. There is also a small, yet noticeable churn region developing in the bottom part of the pipe. This water moves with a higher velocity as it is not subjected to the boundary layer near the wall (no-slip condition). As water is added and quality continues to decrease, the flow shifts to an annular and churn mixture. A thick water layer with ripples is still visible on the pipe walls, but a pronounced churn regime is also seen in the bottom section of the pipe. Images at medium-low air mass fraction (top row, right-middle), show better mixing than images at high air mass fraction, however, the flow is still far from homogenized. An image at 30 psia and lower air mass fractions is not provided in Figure 15 due to the significant performance degradation in the Terry turbine at such conditions.

The middle row in Figure 15 shows images of the two-phase flow entering the turbine over the range of air mass fractions tested at 50 psia inlet pressures. At high air mass

fractions (middle row, left image), the flow is again annular with the water largely adhered to the pipe wall with some ripples visible. The flow is visibly churned at high-moderate air mass fractions (middle row, left-middle image) but still has most of the water concentrated in the bottom half of the pipe. The increase in water droplets suspended in the freestream flow as compared to 30 psia is due to the increase in water mass necessary to maintain a constant air mass fraction as the pressure increases. At low-moderate and low air mass fractions, (middle row, right-middle and right images respectively), the flow is well within the churned regime. The majority of the water is suspended in the free stream away from the walls. The flow is less separated along the vertical direction than at 30 psia, as significant amounts of water are visible in the upper sections of the pipe.

The final row in Figure 15 shows various images of the two-phase flow over the range of air mass fractions tested at 70 psia inlet pressures. As before, the flow is annular at 95% air mass fraction (bottom row, left image) with the liquid primarily adhered to the pipe wall and visible ripples at high air mass fractions. The flow is on the border of the annular and churn regimes at medium-high air mass fractions (bottom row, left-middle image). Some liquid is flowing along the wall, while a significant portion is also flowing in the air stream. As the air mass fraction continues to decrease the flow transitions to a more solidly churned regime. At low-moderate and low air mass fractions (bottom row, right-middle and right images respectively), more water is seen flowing through the pipe and is suspended in the air stream. All of the images shown in the bottom row of Figure 15, taken at 70 psia inlet pressure, show an even vertical distribution of the water inside of the pipe. Body forces have a severely diminished effect at such high pressures and velocities.

When comparing the images at the same air mass fraction across the various inlet pressures, different trends are noticed. At 95% air mass fraction, the flow is in the annular regime with a significant portion of the water adhered to the wall at all three pressures. As the pressure increases, the ripples in the water layer adhered to the wall appear smaller and more spatially dense. This suggests a thinner water surface layer and more water flowing through the pipe as a mist in the air stream. At 60% air mass fraction, the flow generally seems to be in an annular to churn transitional regime. As pressure increases, the flow is more churned and coalesced into smaller beads as more water is visibly mixed with the flowing air in the pipe. At 30% air mass fraction, the flow is still in the annular to churn transition, but closer toward the churned side. As the pressure increases, there is a diminishing water layer adhered to the wall and a more vigorous churn flow with smaller droplets. Finally, at 5% air mass fraction, the flow is well within the churned regime. The main difference due to the pressure change is the vertical uniformity of the water distribution at 70 psia as compared to 50 psia.

A compilation of the high-speed videos of the two-phase flow for a given pressure at varying air mass fractions are provided in the supporting files. The original images were taken at 400 fps and are replayed at 24 fps or 6% of real speed. The video images help to support the previously discussed observations in the static pictures. In particular, the videos show a much clearer distinction between water that is adhered to the outer pipe wall and water that is suspended in the free stream air due to the significant velocity difference. This difference is especially useful in evaluating the transition from the annular to the churned

flow regime. Similarly, the videos show the substantial velocity increase of process fluid due to the elevated pressures through the flow visualization section.

In general, the two phases were fairly well mixed despite flow through a horizontal piping section. The flow is mixed at lower static pressure, but the water distribution is skewed toward the bottom of the pipe. This is due to the disparity in body forces on the fluids because of the large difference in density. At higher pressures, body forces, which separate the flow, have a diminished effect due to the elevated mass flow rates and velocities through the visualization section which cause greater flow homogenization. Additionally, the increase in pressure leads to smaller water beads within the pipe. The elevated pressures induce higher shear stresses which tend to break slugs into smaller beads. For this study, qualitative visual analysis yields better results than two-phase flow maps in classifying the two-phase flow regimes.

8. EXPERIMENTAL RESULTS AND ANALYSIS

The experimental results of the valve testing and of the Terry turbine's performance are presented below. The valve testing results show the flow coefficient, C_v, at different valve positions while using air or water as the process fluid. Meanwhile, the turbine testing results present the overall performance maps of the Terry GS-2 turbine for single-phase (100% air) and two-phase (5 – 95% air mass fraction) flow tests at pressures ranging from 20 psia to 70 psia. Torque and efficiency curves, as a function of rotational speed, are generated to characterize Terry turbine performance.

The valve data is presented in terms of number of handwheel or positioning nut revolutions from the closed position, as it is a more useful parameter from an operator standpoint. Stem withdrawal, however, is a more precise parameter for describing stem position. Figure 19 and Figure 20 show the valve stem withdrawal as a function of handwheel and positioning nut revolutions, respectively. Both the Trip-Throttle Valve (TTV) and Governor Valve (GV) exhibit a linear relationship between these two parameters over the range of the valve.

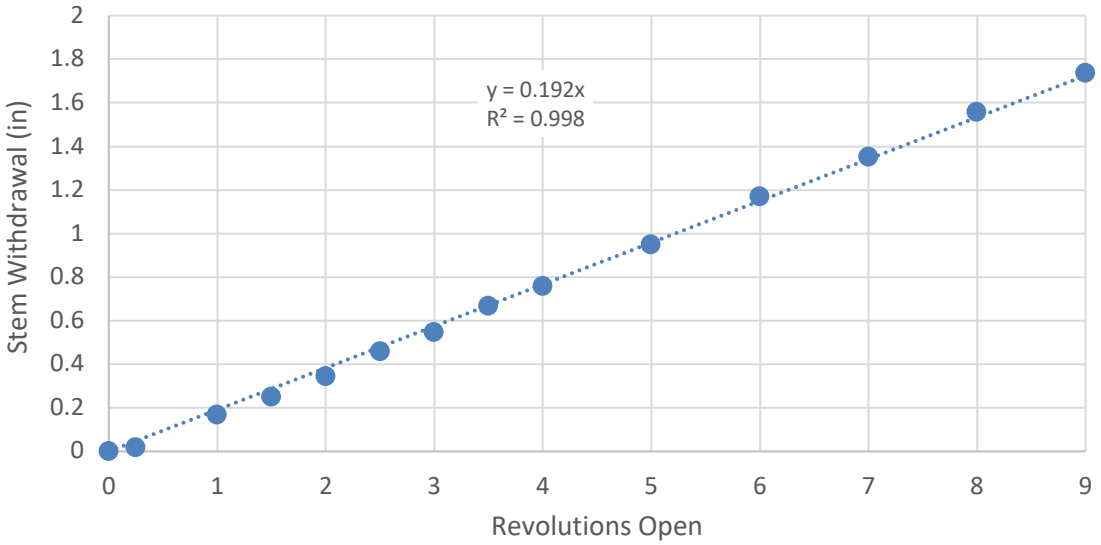

Figure 19: Stem Withdrawal vs. TTV Handwheel Revolutions

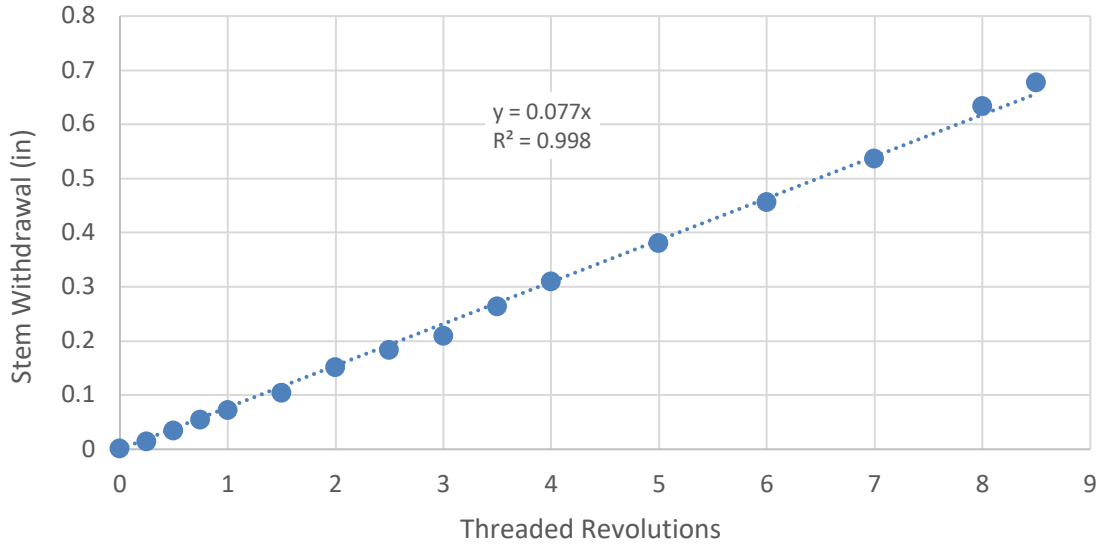

Figure 20: Stem Withdrawal vs. GV Positioning Nut Revolutions

8.1. Trip-Throttle Valve

As described in the Procedure section while using air as the process fluid, several data points were recorded at a given valve position by incrementally closing the back-

pressure gate valve, which in turn varied the dimensionless pressure drop across the test specimen. As expected, there is a linearly decreasing relationship between the compressible flow coefficient (YC) value and the dimensionless pressure drop (x). Figure 21 displays this trend with TTV when testing at 3 handwheel revolutions open.

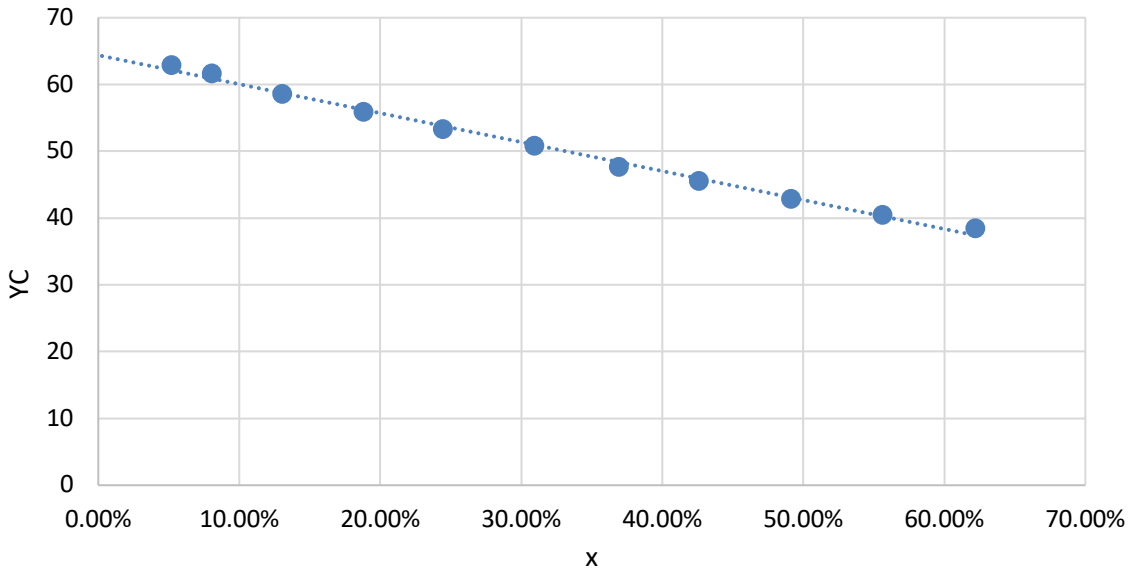

Figure 21: TTV Compressible Flow Coefficient (YC) vs. Dimensionless Pressure Drop (x) at 3 Revolutions Open (Air)

Data at four and fewer revolutions open shows similar linear results. Above four revolutions, the data becomes erratic and inconclusive. As the test specimen is opened further to allow more air to flow, a greater volume of air is needed to maintain a given dimensionless pressure drop. Facility limitations on air capacity restrict the maximum achievable dimensionless pressure drop to approximately 20% at five revolutions open and 12% at the fully open position, as compared to 62% at three revolutions. The smaller

dimensionless pressure drop window leads to a limited understanding of valve behavior at higher stem positions, which likely is causing the erratic data.

On the compressible flow coefficient vs. dimensionless pressure drop graph, the linear best fit line is extrapolated back to the vertical axis. At this intersection, $Y = 1$, and the C_v value can be read directly. From Figure 21, the flow coefficient, C_v, at three revolutions open is 64 ± 1. A similar analysis is used to calculate the flow coefficient at other valve positions. Combining the results, Figure 22 shows the experimentally determined flow coefficient at valve positions between one and four revolutions open.

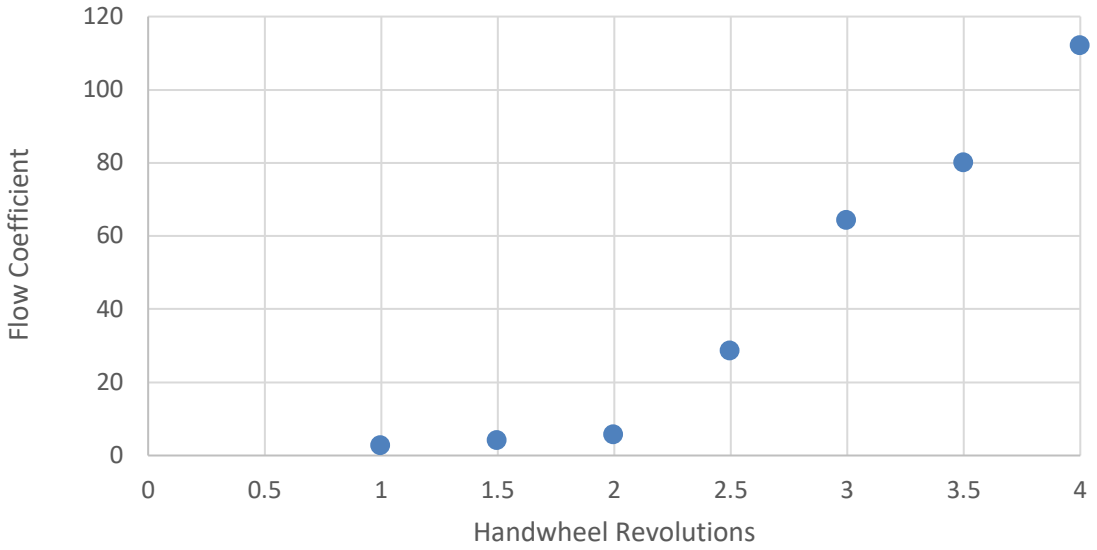

Figure 22: TTV Flow Coefficient vs. Handwheel Revolutions (Air)

The results suggest either a parabolic or a dual linear regime relationship between stem withdrawal and flow coefficient. The first three points (1, 1.5, 2 revolutions) display a distinct linear pattern, with a relatively small slope. The remaining points suggest a second

linear regime with an increased slope. The transition point between the two regions appears to be at a stem withdrawal around 0.34 inches or approximately two handwheel revolutions. The increase in the rate of change of the flow coefficient as a function of handwheel revolutions may be from the changing position of the internal plug mechanism. As shown in Figure 3, most plug valves have a conically shaped plug (label 44) that moves up and down to throttle the flow through the valve seat (label 23). At and below two revolutions, the tip of the plug mechanism is still crossing the horizontal plane at the top face of the valve seat. This limits the cross-sectional fluid flow area to the lateral surface area of a conoid slice. As the valve opens, however, the plug moves further away from the valve seat and the tip no longer crosses the plane of the valve seat face. At this point, the cross-sectional fluid flow area is circular and has a greater rate of change.

Figure 23 compares the flow coefficient, when using water, to the valve stem withdrawal. As with the air case, there are two distinct linear regions with an increase in the rate of change of the flow coefficient around 0.35” of stem withdrawal.

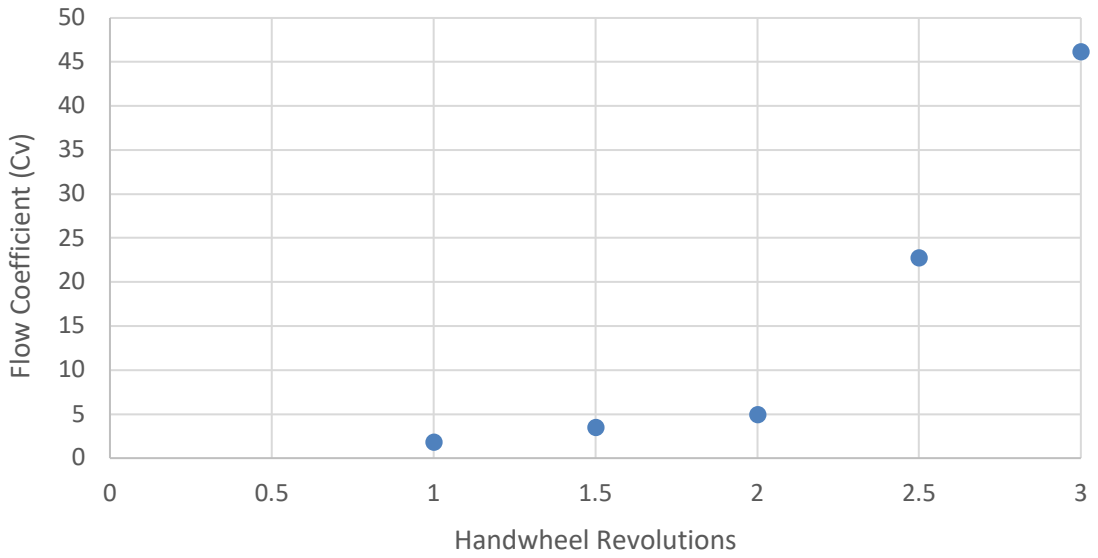

Figure 23: TTV Flow Coefficient vs. Handwheel Revolutions (Water)

For each position, the flow coefficient calculated using air as the process fluid is greater that when using water as the process fluid. Table 2 summarizes the flow coefficient values using both air and water, the x_T value, and the ratio of C_v air to C_v water, for the TTV. Instrument and calculated parameter uncertainties are summarized in the Appendix.

Table 2: Summary of TTV Flow Coefficient Values

Revolutions	Stem Withdrawal (in)	C_v air	x_T	C_v water	C_v air/C_v water
1	0.17	2.6 ± 0.1	0.85 ± 0.1	1.9 ± 0.1	1.5
1.5	0.25	4.1 ± 0.1	0.64 ± 0.09	3.6 ± 0.2	1.2
2	0.34	5.8 ± 0.1	0.57 ± 0.05	5.0 ± 0.2	1.2
2.5	0.46	29 ± 0.6	0.49 ± 0.06	23 ± 1	1.3
3	0.55	64 ± 1	0.49 ± 0.04	46 ± 1	1.4
3.5	0.67	80 ± 2	-	-	-
4	0.76	112 ± 3	-	-	-

8.2. Governor Valve

Analysis of the GV is similar to that of the TTV. When plotting the measured compressible flow coefficient (*YC*) values against the dimensionless pressure drop for various back pressures at a given valve position, the data, again, fall into the expected, consistent linear trend. Figure 24 shows this trend on the GV when the positioning nut is three revolutions from the closed valve position.

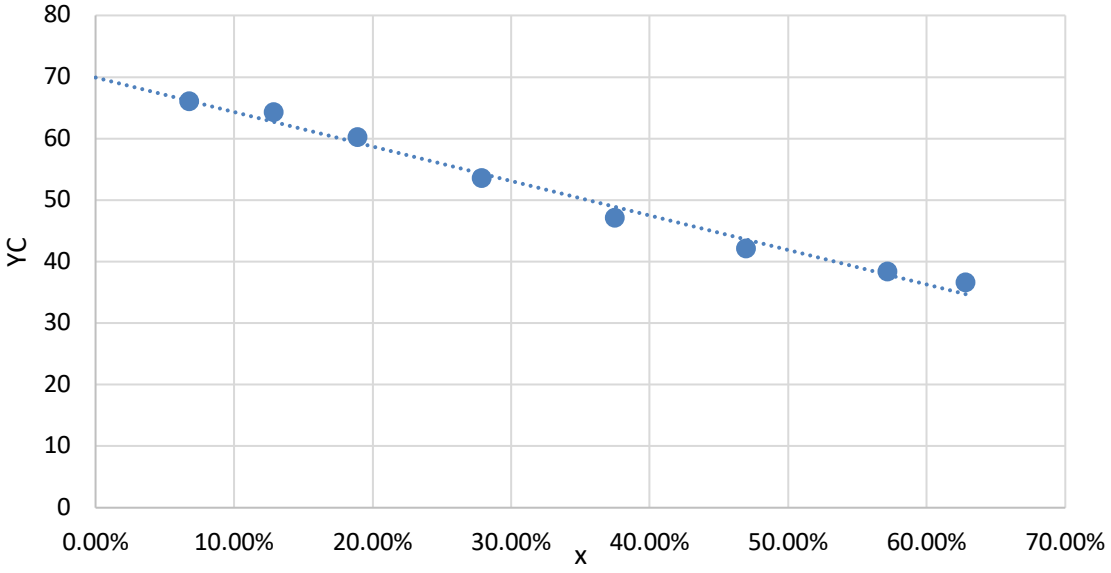

Figure 24: GV Compressible Flow Coefficient (YC) vs. Dimensionless Pressure Drop (x) at 3 Revolutions Open (Air)

The compressible flow coefficient vs. dimensionless pressure drop (*YC* vs. *x*) data for the governor valve shows expected linear results at and below five revolutions. Similar to the TTV, when the positioning nut is at more than five revolutions, the data becomes erratic and inconclusive. This is again likely due to the smaller available dimensionless pressure drop range for testing, due to facility limitations. For the GV, at three revolutions

open, the maximum dimensionless pressure drop is about 63%, while it is only 26% at six revolutions and 18% at the fully open position. The C_v value for three revolutions, read directly from the graph, is 70 ± 3. Figure 25 shows the combined C_v values for the various GV positions tested.

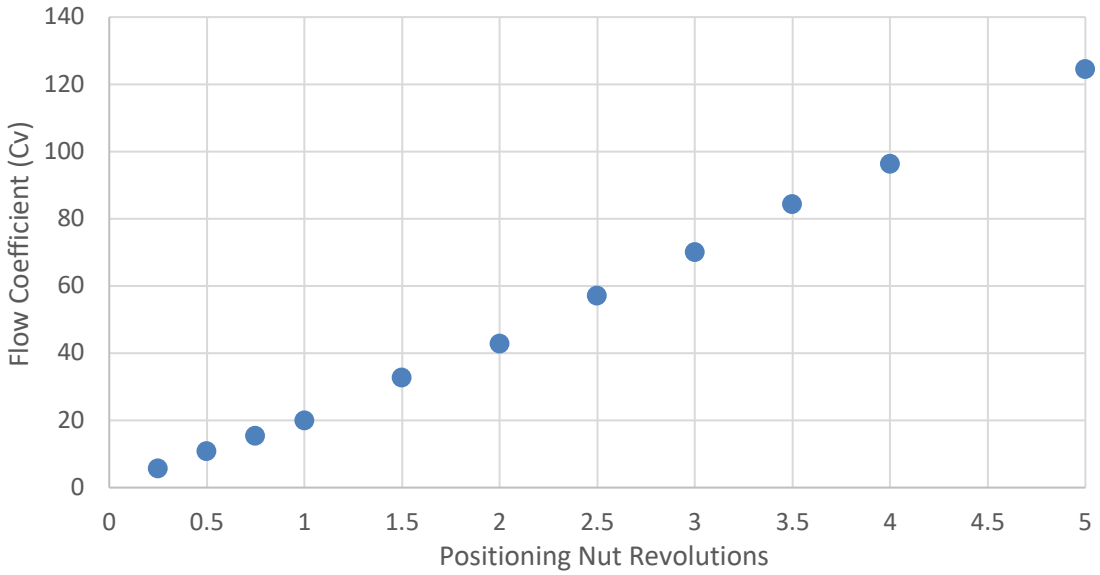

Figure 25: Flow Coefficient vs. GV Positioning Nut Revolutions (Air)

Unlike the TTV, the flow coefficient shows a single distinct linear correlation with stem withdrawal. A similar single linear trend, as shown in Figure 26, appears when evaluating the GV flow coefficient with water. This linear behavior is imperative for the GV as it is the main mechanism for controlling the speed of the turbine. Non-linear or piecewise correlations could severely complicate the controlling mechanism and make turbine controls less effective.

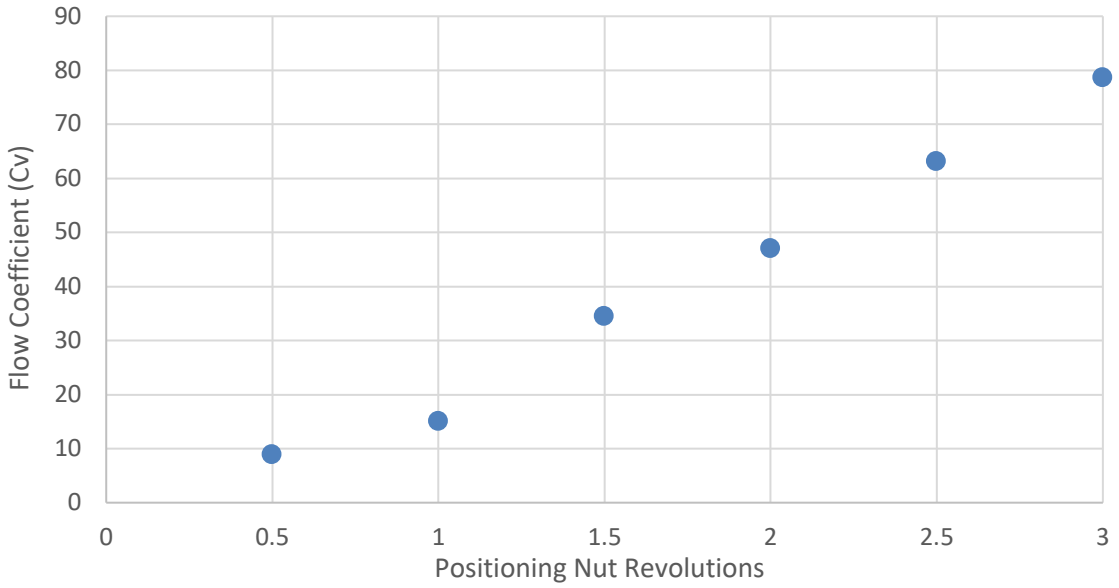

Figure 26: Flow Coefficient vs. GV Positioning Nut Revolutions (Water)

Although the GV shows a similar linear trend when tested with either air or water, the trends have differing slopes, with the water data being steeper. The flow coefficient values using both air and water, the x_T value, and the ratio of C_v air to C_v water, for the GV, are summarized in Table 3.

Table 3: Summary of GV Flow Coefficient Values

Revolutions	Stem Withdrawal (in)	C_v air	x_T	C_v water	C_v air/C_v water
0.25	0.01	5.5 ± 0.3	0.45 ± 0.1	-	-
0.5	0.03	10.8 ± 0.4	0.48 ± 0.08	8.9 ± 0.1	1.2
0.75	0.05	15 ± 1	0.46 ± 0.07	-	-
1	0.07	20 ± 1	0.46 ± 0.07	15.0 ± 0.5	1.3
1.5	0.10	33 ± 1	0.45 ± 0.08	34 ± 1	0.95
2	0.15	43 ± 2	0.43 ± 0.08	47 ± 2	0.91
2.5	0.18	57 ± 3	0.43 ± 0.08	63 ± 2	0.90
3	0.21	70 ± 3	0.42 ± 0.07	79 ± 3	0.89
3.5	0.26	84 ± 3	-	-	-
4	0.31	96 ± 3	-	-	-
5	0.38	124 ± 4	-	-	-

8.3. Turbine – Single Phase Flow

As previously mentioned, an air heater was used to pre-heat the air stream entering the Terry turbine in order to help bring the exit temperatures above the freezing point of water. The addition of the air heater raised the inlet temperatures by 25-35 °F and raised exit temperatures by 5-15 °F, depending on other test parameters. This successfully elevated the exit temperature above the freezing point for the single-phase air trials at 20, 30 and 50 psia. The exit temperature for the 70 psia inlet trials remained below freezing.

Figure 27 and Figure 28 show the performance parameters, torque and efficiency, of the Terry GS-2 turbine at 100% air fraction. Data sets for trials with and without the air heater are displayed. Figure 27 shows no appreciable difference on torque between the tests with and without the air heater while holding the inlet pressure constant, while Figure 28, on the other hand, shows noticeable differences in efficiency when including the air heater. The

trials utilizing the preheated air have an increased efficiency compared to those without preheated air. This is because the heated air has a greater expansion potential than the non-heated air.

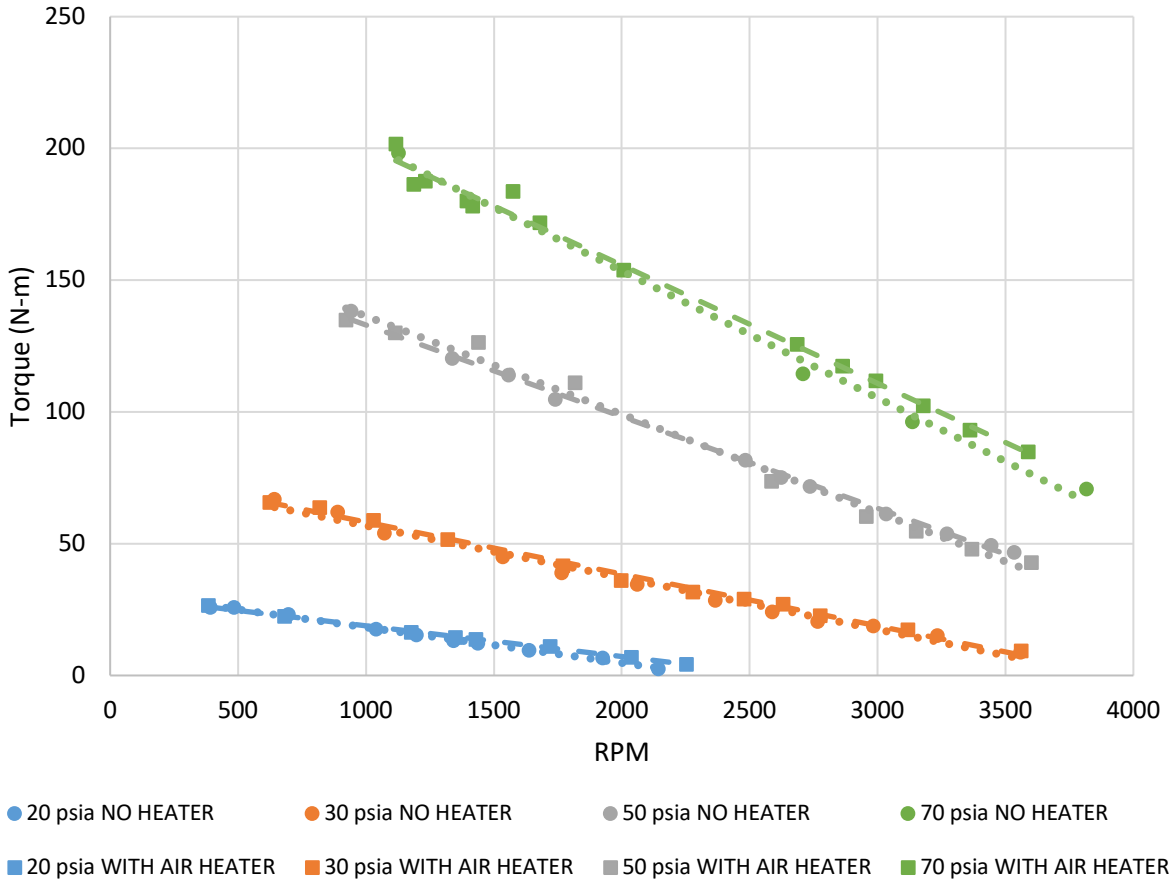

Figure 27: Torque vs RPM for 100% air fraction

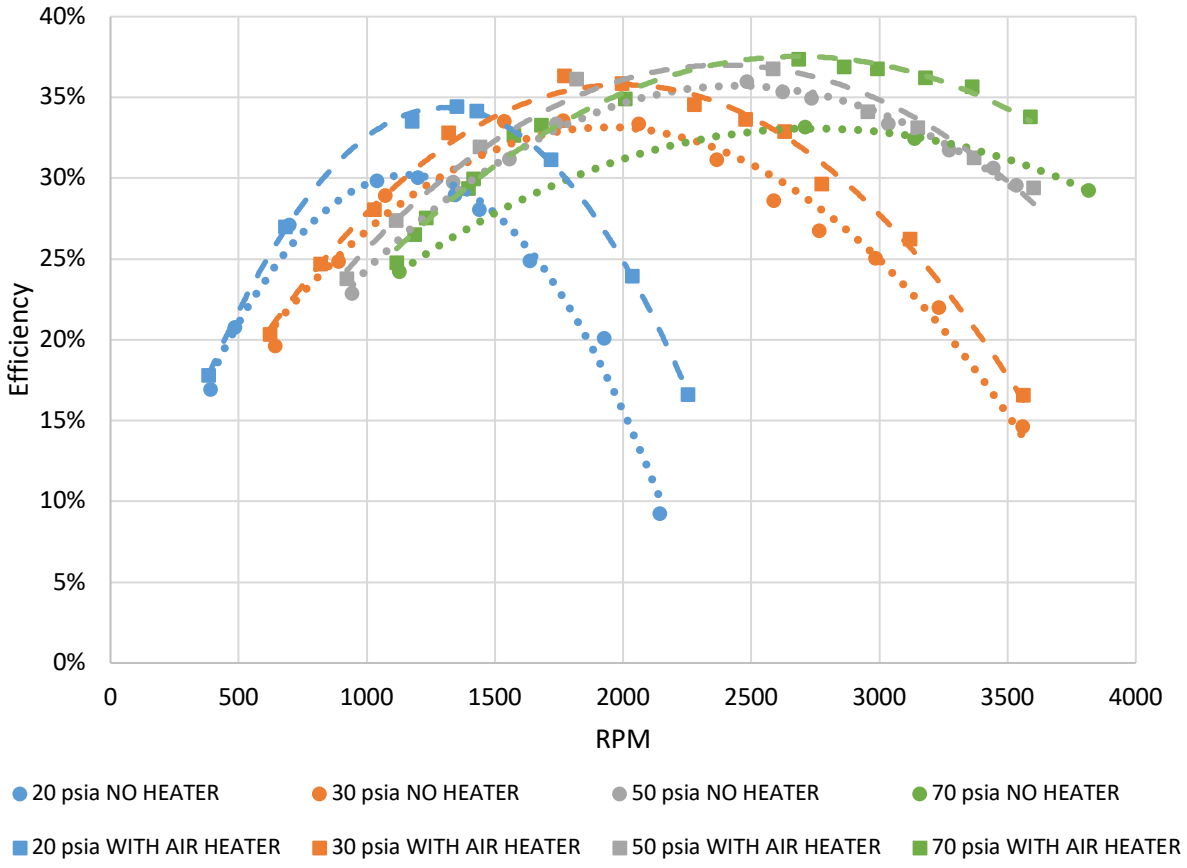

Figure 28: Efficiency vs. RPM for 100% air fraction

As the inlet pressure increases, there is an increase in fluid power entering the turbine, which increases the shaft output torque. For the preheated air data sets, the peak efficiencies in Figure 28 seem to increase with increasing inlet pressure until reaching a maximum efficiency of 37-38% at 50 and 70 psia. The reduced peak operating efficiency at 20 and 30 psia is likely due to the pressure ratio across the converging-diverging turbine nozzles. At 20 psia, the pressure ratio across the turbine nozzle is not large enough to choke the flow; therefore, the flow slows in the diverging section of the nozzle. The reduced flow velocity entering the turbine buckets causes the decreased efficiency. At 30 psia, the

pressure ratio across the turbine nozzle is enough to choke the flow but is not sufficient to accelerate the flow to the designed supersonic nozzle exit velocity. The over-expanded flow passes through a shock wave, which reduces flow velocity and thus decreases turbine efficiency. Flows at 50 and 70 psia have large enough pressure ratios to accelerate the flow to the nozzle design point, and therefore, have the largest peak efficiencies.

8.4. Turbine – Multiphase Flow

Shakedown testing showed that the Terry GS-2 turbine will begin rotating when subjected to an inlet pressure of approximately 17 psia. The lower end test pressure was set at 20 psia in order to better evaluate performance at the lower end of the turbine's operational capabilities.

The output shaft torque and turbine efficiency at 20 psia inlet pressure at varying air mass fractions are given in Figure 29 and Figure 30. The torque output from the turbine follows a linearly decreasing trend with increasing rotational speed. The efficiency follows a parabolic trend with a peak efficiency at a moderate rotational speed for the given conditions. The peak or best efficiency point (BEP) moves up and toward the right with increasing air mass fraction. The series of torque curves and efficiency curves both collapse down as the air mass fraction is varied, following expected turbine performance trends. As anticipated, the addition of water to the flow degrades the turbine's performance as it reduces the amount of energy the turbine can extract from the process fluid. Air mass fractions below 50% were not tested as the turbine was not able to extract enough energy to produce meaningful results.

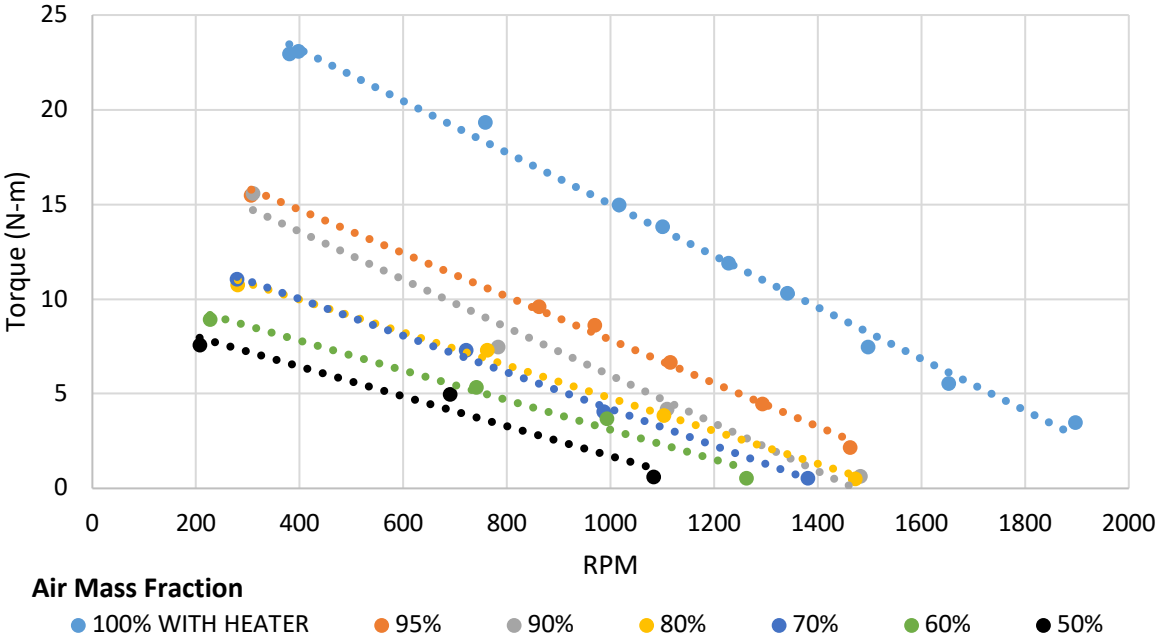

Figure 29: Two-Phase Shaft Output Torque at 20 psia Inlet Pressure

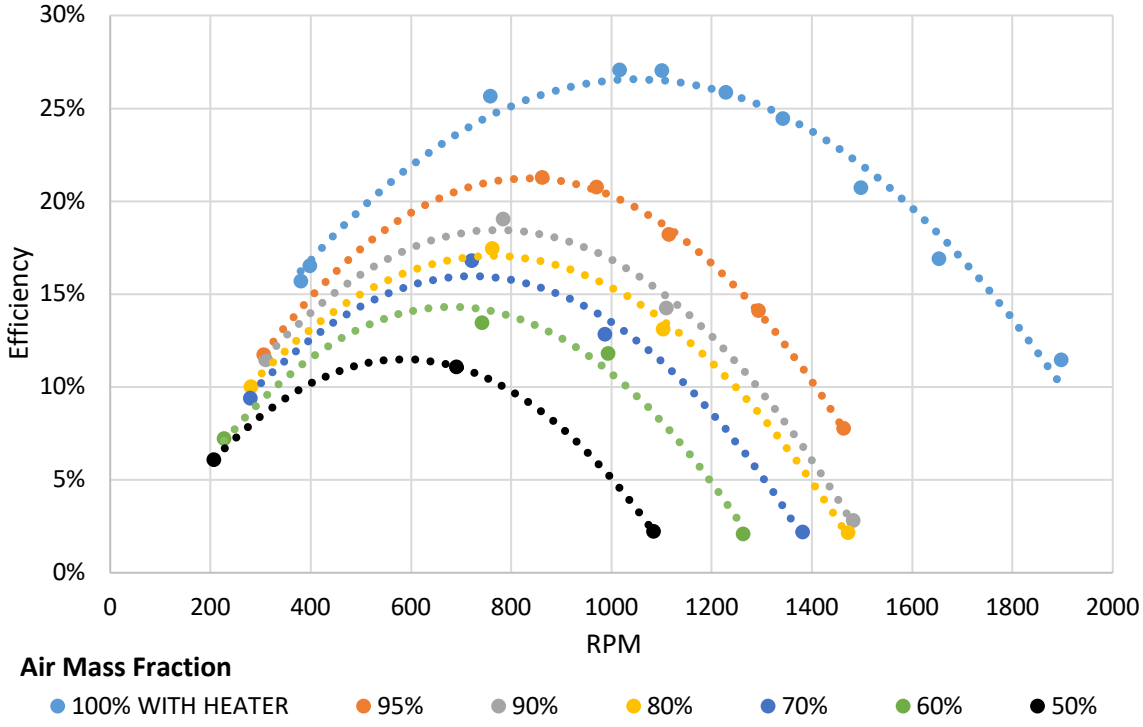

Figure 30: Two-Phase Turbine Efficiency at 20 psia Inlet Pressure

Figure 31 and Figure 32 show the torque and efficiency plots at 30 psia (0.21 MPa) inlet pressure. For tests at the same air mass fractions, both the output torque and efficiencies were higher at 30 psia than at 20 psia due to the increase in available energy injected into the turbine. Some lower air mass fractions were also able to be tested because of the increase in available energy. Overall, at 30 psia the Terry turbine exhibits similar trends and behaviors to those seen at 20 psia.

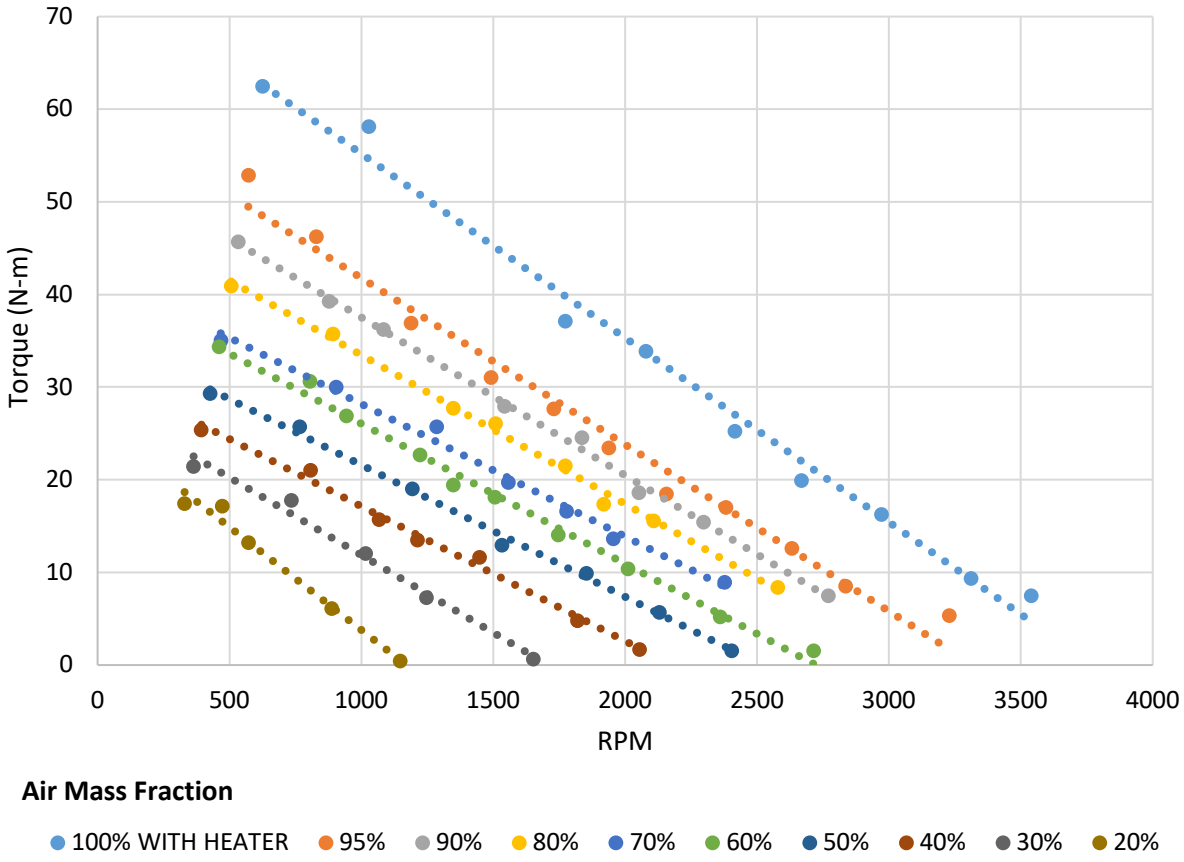

Figure 31: Two-Phase Shaft Output Torque at 30 psia Inlet Pressure

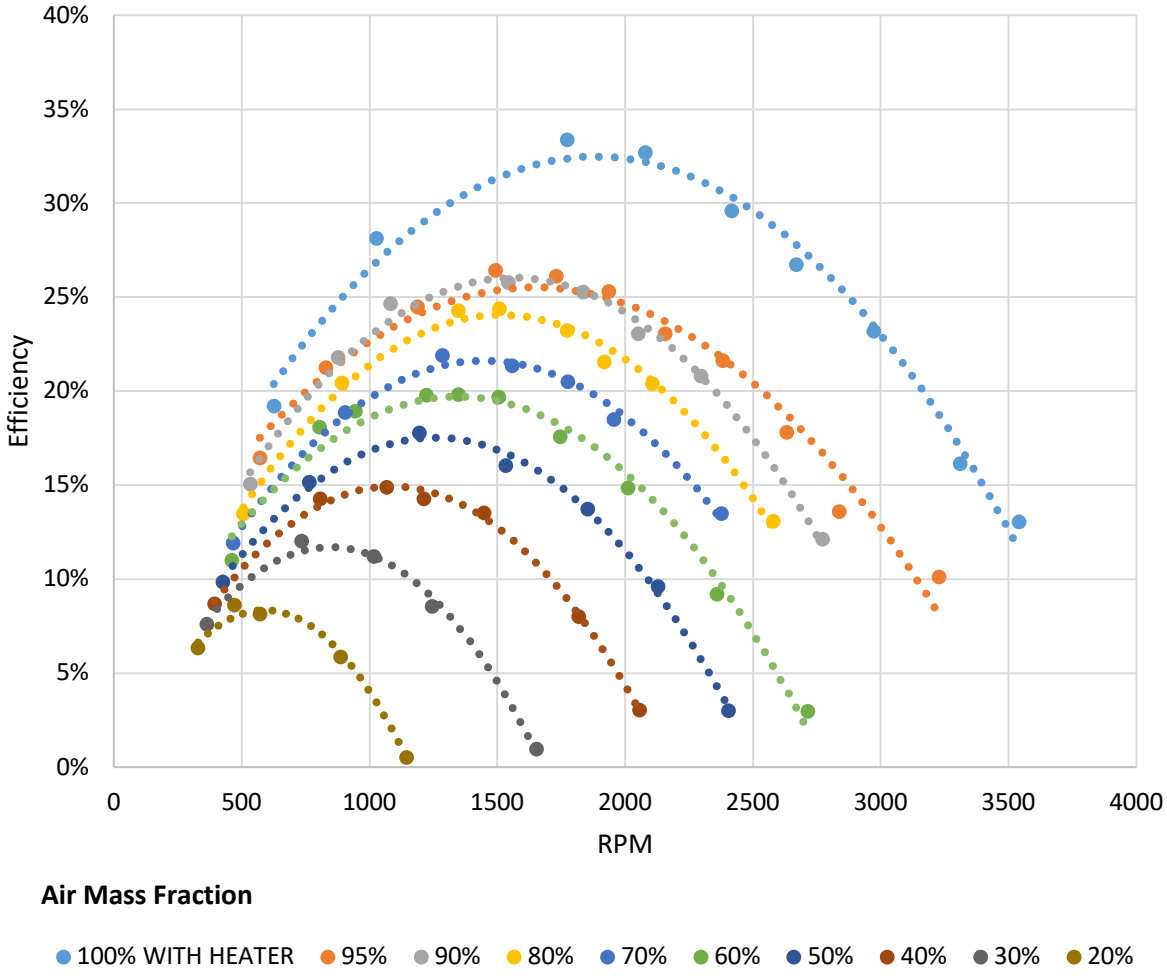

Figure 32: Two-Phase Turbine Efficiency at 30 psia Inlet Pressure

The upper turbine inlet pressures of 50 and 70 psia (0.345 and 0.48 MPa) were also tested. Figure 33 to Figure 36 show the performance maps of turbine output torque and turbine efficiency at these elevated pressures. Again, the increased inlet pressures lead to higher torques and efficiencies from the turbine. Air mass fractions as low as 5% were also able to be tested because of the increased pressure. For the most part, the turbine performance was similar to that at 20 and 30 psia; however, performance deviated from

expected trends in one significant way. At 50 and 70 psia, high two-phase air mass fractions resulted in suppressed or lower than expected output torque and efficiency values, as denoted by the long-dashed trendlines in Figure 33 to Figure 36.

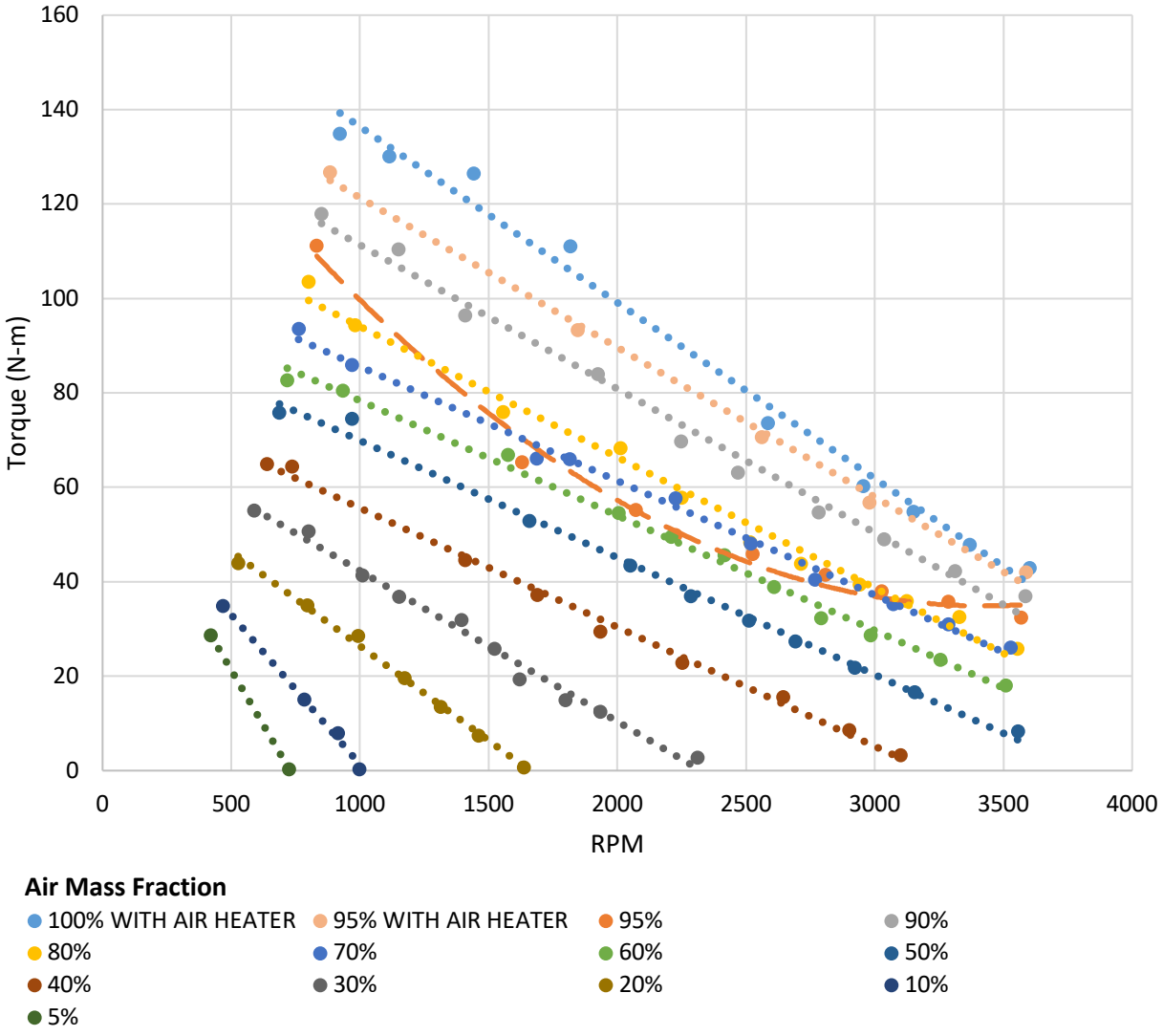

Figure 33: Two Phase Shaft Output Torque at 50 psia Inlet Pressure

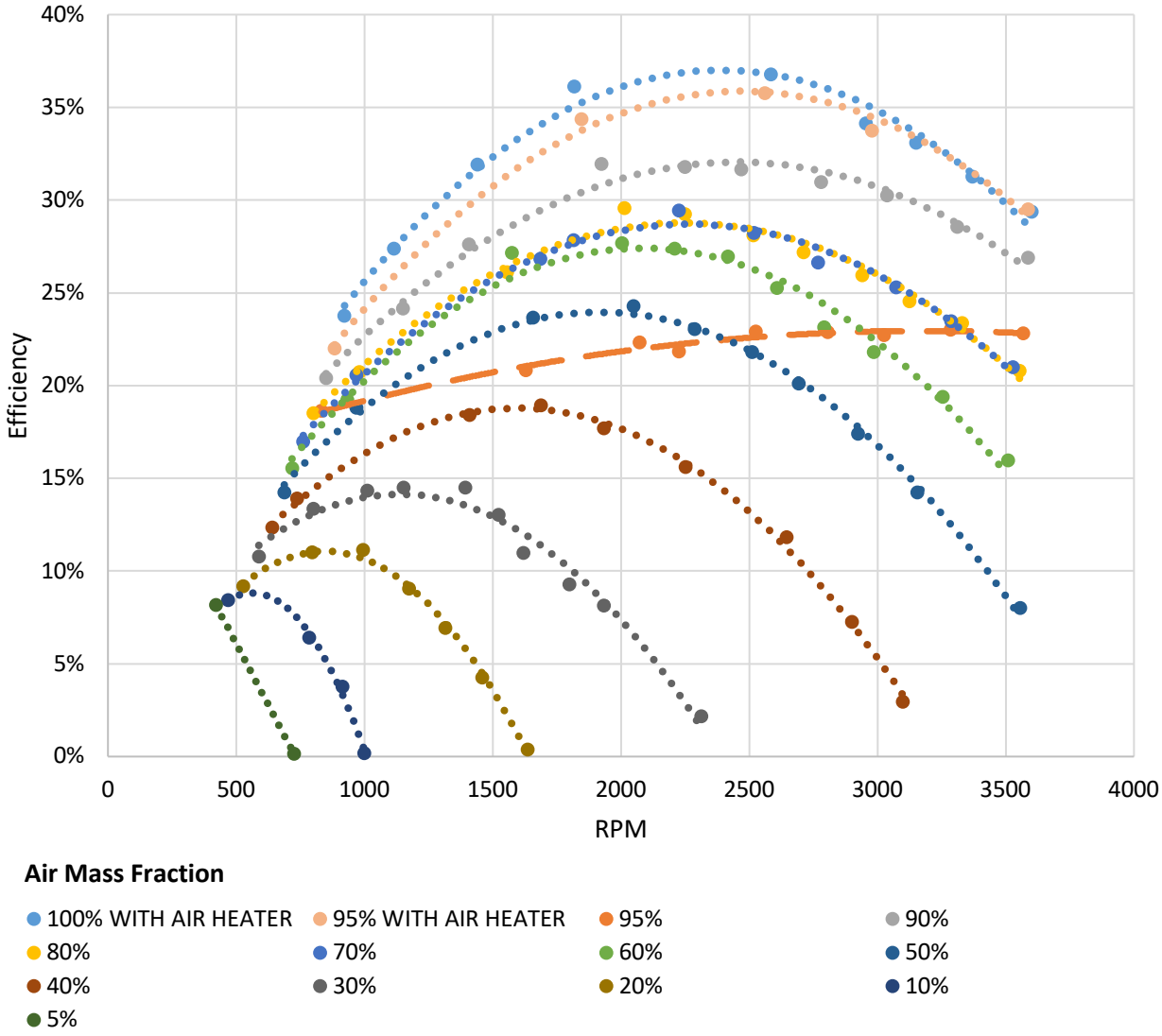

Figure 34: Two-Phase Turbine Efficiency at 50 psia Inlet Pressure

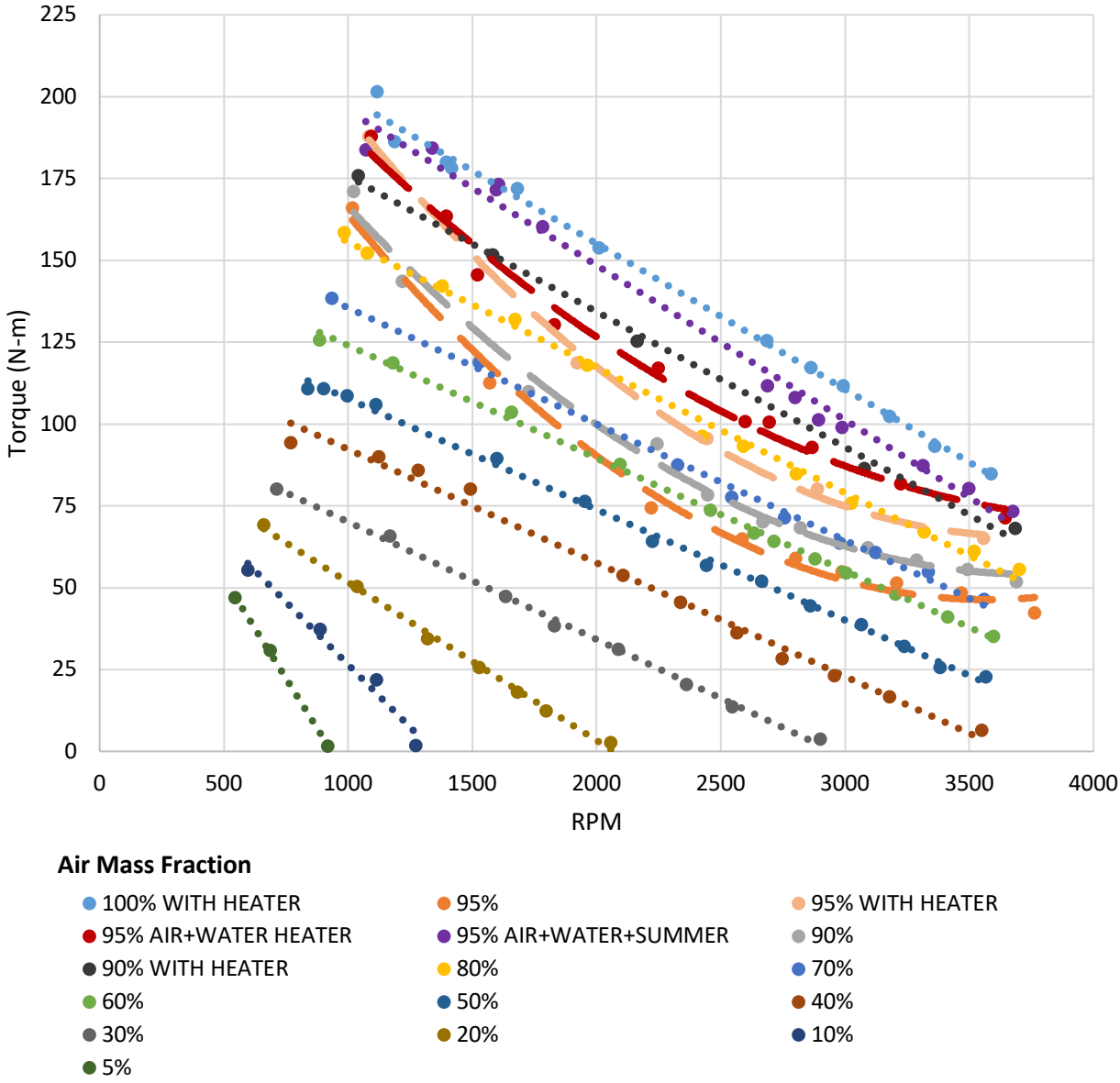

Figure 35: Two-Phase Shaft Output Torque at 70 psia Inlet Pressure

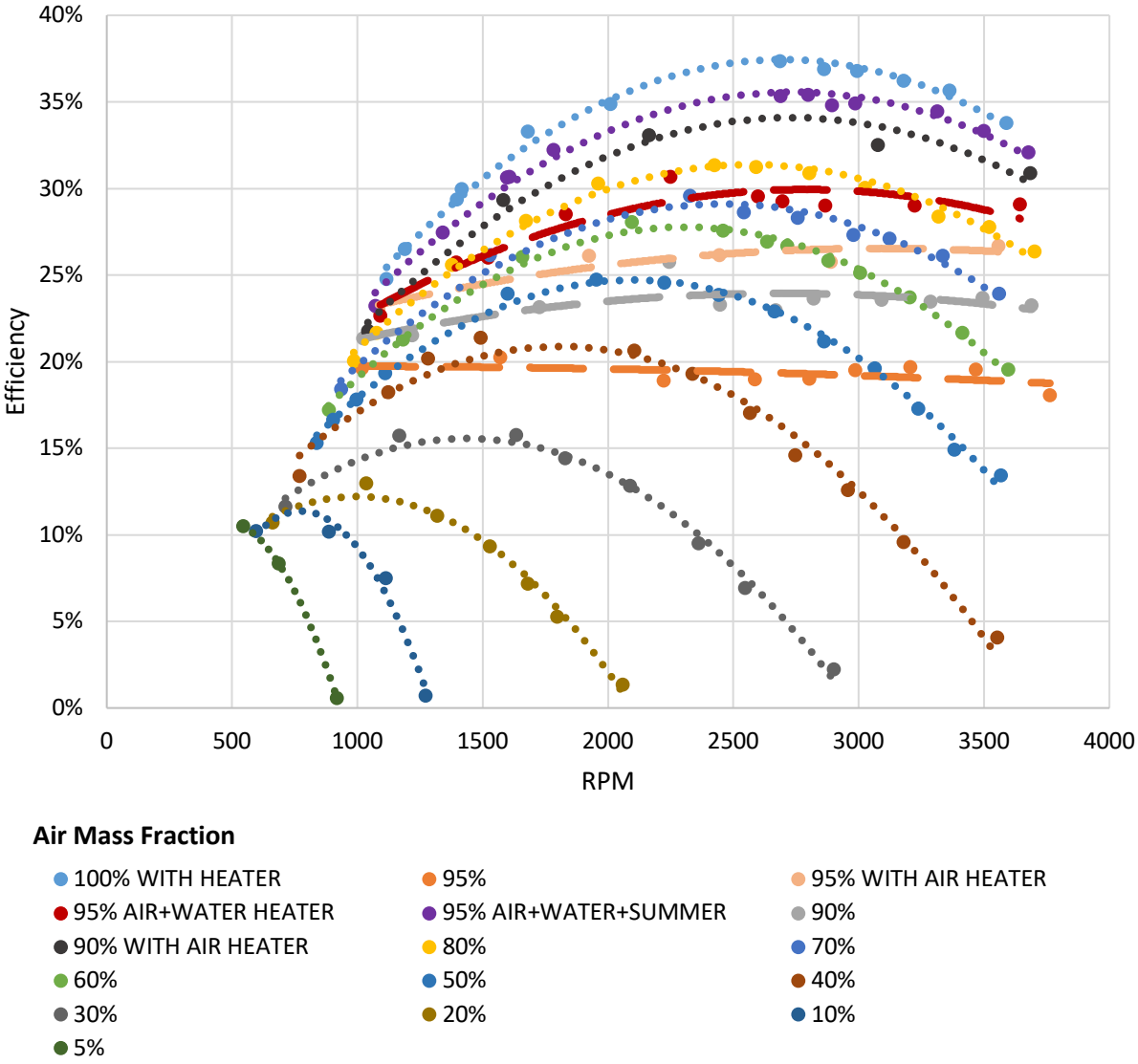

Figure 36: Two-Phase Turbine Efficiency at 70 psia Inlet Pressure

This suppressed behavior was observed at 50 psia, 95% air mass fraction, and at 70 psia, 90-95% air mass fraction. The unexpectedly low torques and efficiencies were repeatable during testing. Investigation showed that the phenomenon was related to the inlet process fluid temperatures. It is suspected that the formation of ice inside the turbine causes the performance drop.

This suppressed behavior was not observed at air mass fractions of 80% and lower, likely due to the heat capacity of water. If the turbine inlet pressures continued to increase, this lower threshold would likely continue to decrease as well due to the larger temperature drops across the nozzle. Below the threshold, the water has sufficient heat capacity to supply thermal energy to the surrounding air as it expands while maintaining its liquid state. Above the threshold, the water does not have sufficient heat capacity to provide heat to the expanding air while remaining a liquid. The large pressure and temperature drop and associated heat transfer from water to air causes the water to freeze at high air mass fractions.

To prevent the suppressed output, the air heater was again employed to preheat the inlet air stream. This additional heat improved the data sets taken at 50 psia, 95% air mass fraction and 70 psia, 90% air mass fraction by raising the output torques and efficiencies to within their expected ranges. The data set at 70 psia, 95% air mass fraction improved, but the system still needed more heat. Therefore, a household, instant hot-water heater was used to preheat the water stream as well.

The water heater also contributed to an improved turbine performance, but the unexpectedly low torque persisted due to the winter weather combined with the rigorous testing schedule. Interpolating from the “100% with air heater” and “90% with air heater” data sets at 70 psia inlet pressure, the expected BEP for the 95% air mass fraction inlet condition was 36%. After waiting for warmer weather in late spring, this same data set was tested again, using both the air and water heaters to preheat the incoming flow. In Figure 35 and Figure 36, this data set is labeled “95% air + water + summer”. The 40-50 °F exterior

temperature increase led to a significant rise in the inlet flow temperature and the torque and efficiency curves fell within expected ranges. The BEP was 35.5%, near the previously expected value. Figure 37 shows the peak operating efficiency increase as the inlet temperature increases. The first point corresponds to the non-heated "95%" data set; the second and third points correspond to the "95% with air heater" and "95% air + water heater" data sets respectively, while the last point corresponds to the "95% air + water + summer" data set.

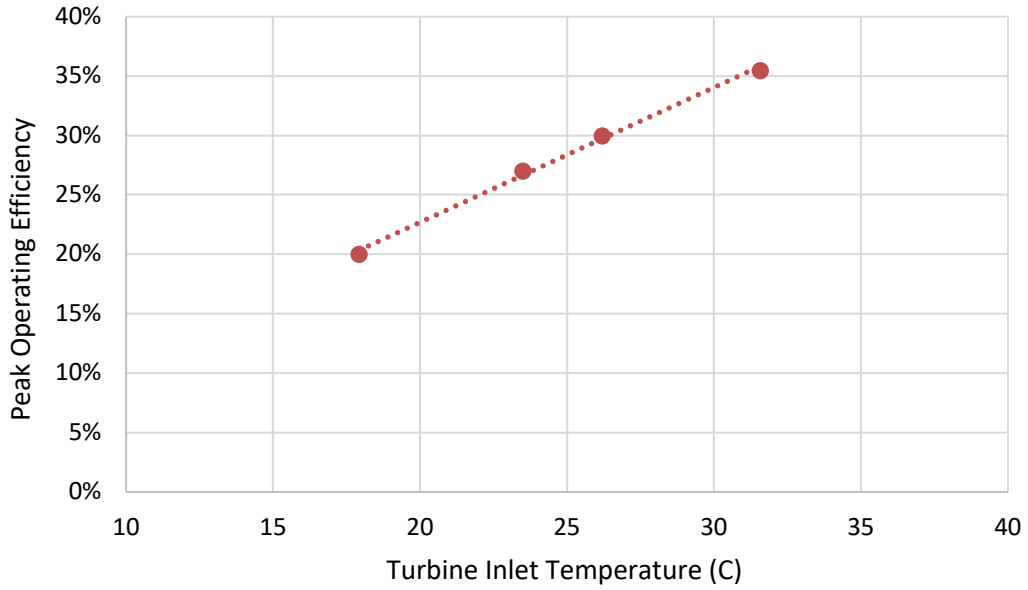

Figure 37: Peak Operating Efficiency vs. Inlet Temperature given a 70 psia, 95% Air Mass Fraction Inlet Flow

A smaller than expected temperature drop at higher air mass fractions is further evidence for icing within the turbine. Figure 38 shows the dimensionless temperature drop across the turbine as a function of air mass fraction. The temperature drop across the turbine increases smoothly with increasing air mass fraction, except around 95%, depending on the

inlet pressure. Within a phase regime, the temperature change is expected to be proportional to the heat transferred. Around 95% air mass fraction (circled on the graph), the temperature drops are suppressed since the temperature stays constant during phase change as enthalpy of fusion heat is released.

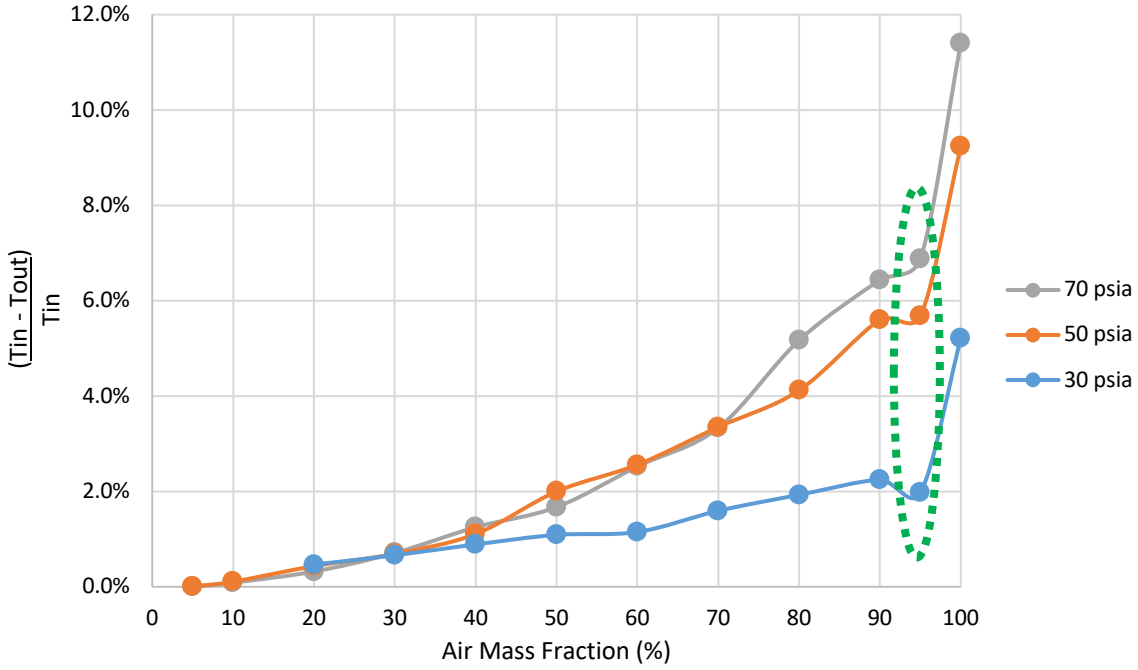

Figure 38: Dimensionless Temperature Drop by Air Mass Fraction[1] Highlighting Suppressed Temperature Drops at 95% Air Mass Fraction

8.5. Bearing Friction

To better understand the role that the bearings play in the performance of the turbine, it is important to understand the drag friction as a function of rotational speed. The Terry

[1] The data at 50 psia, 95% air mass fraction, and 70 psia, 90% air mass fraction, includes the use of the air heater. The data at 70 psia, 95% air mass fraction includes the use of the air and water heater during the winter months. All other multiphase data does not include any pre-heaters.

GS-2 turbine utilizes fluid film journal bearings to support the rotating shaft. The drag friction is the force associated with shearing the oil film at the given rotational speed. This parameter quantifies the bearing energy losses (excluding oil churning losses) associated with rotating the turbine.

The drag friction is measured as torque using the water brake dynamometer without a water load while the turbine is subject to single-phase air flows. The required start-up torque is 4.1 ± 0.1 N-m. When operating under steady-state conditions, the drag friction increases with rotational speed over the operating range of the turbine. As shown in Figure 39, at 500 RPM, the drag friction is approximately 0.8 N-m, while at 3500 RPM, the drag friction is slightly below 2.5 N-m.

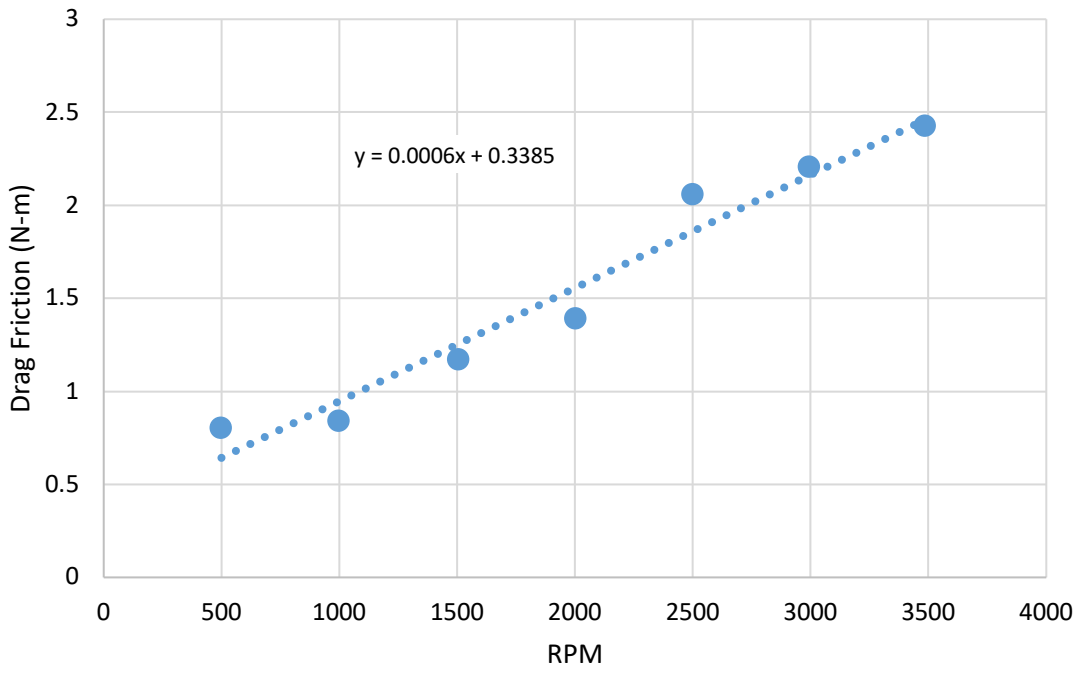

Figure 39: Turbine Drag Friction as a Function of Rotational Speed

The turbine drag friction behavior during a transient condition also yields interesting results. Figure 40 shows the dynamic response of the turbine after the supply air has been abruptly shut off and the turbine is allowed to coast to a stop. As with steady state operation, higher rotational speeds yield elevated drag friction. As the turbine gradually slows, the drag friction diminishes correspondingly. As the turbine approaches its resting point, less lubricating oil is pulled into the journal bearing and the bearing enters the mixed boundary lubrication regime. This transition is indicated by the dashed green oval in Figure 40. This drag friction spike was repeatedly observed during testing shutdowns.

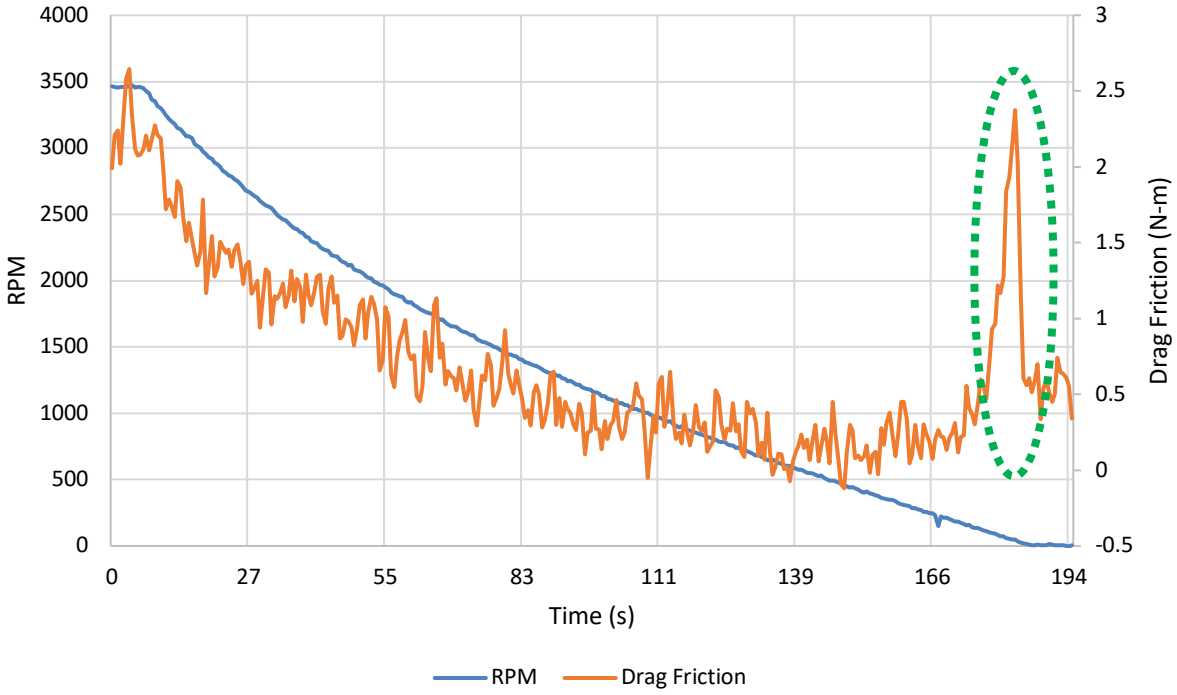

Figure 40: Transient Frictional Drag of a Terry Turbine Coasting to a Stop

8.6. Bearing Housing Temperature Observations

Understanding how heat builds in and dissipates from the turbine bearings may help with investigations of the Terry turbine bearing failure. During single-phase air testing, the bearing housing temperature rose to ~100-105 °F. When injecting small amounts of water (~60-65 °F) to the flow, around 95% air mass fraction, the bearing housing temperature would fall about 10-15 °F within ten minutes. As additional water was added, the bearing housing temperature continued to fall to approximately 70-75 °F at 5-10% air mass fraction.

During multiphase tests, the front seal consistently leaked, especially at low air mass fractions. These leaks raised some concerns that the cool process water, seeping through the front seal, may have been entering the oil reservoir in the bearing housing during the accumulated 75 hours of turbine runtime. However, after opening and inspecting the oil reservoir and repeatedly flushing the sight-glass at the bottom of the reservoir, there was no evidence of water in the lubricating oil. Therefore, the cooling of the bearing housing with increasing water fraction in the flow was likely due to conductive heat transfer through the turbine's main shaft.

9. CONCLUSIONS

RCIC system component testing has been executed on a Terry GS-2 steam turbine and associated valves in a multiphase test loop. This work was aimed at evaluating the operational capabilities of Terry turbines for extended use in nuclear power generation facility cooling systems by experimentally characterizing the turbine's operational performance under multiple operating conditions.

The Trip-Throttle Valve and Governor Valve were each tested individually to experimentally determine their corresponding flow coefficients, C_v. When testing with either single-phase air or water, the TTV showed a bi-linear correlation between stem withdrawal and flow coefficient with the coefficient changing more quickly when the valve was above 0.35" of stem withdrawal or about two handwheel revolutions. The GV, on the other hand, showed a single linear trend between stem withdrawal and flow coefficient for both process mediums. When comparing the process mediums, on the TTV, using air always resulted in a higher flow coefficient at a given valve position; however, on the GV, using air resulted in a higher flow coefficient at and below 1 revolution of opening but above one revolution, the flow coefficient was higher when using water.

A visualization study was performed on the air-water flow entering the turbine. At high air mass fractions, the water phase is largely flowing along the wall resulting in an annular flow regime. As the air mass fraction decreases, the flow transitions to a churned regime with the majority of water beads suspended in the air stream. The effect of increasing pressure is two-fold: higher pressures lead to smaller water beads within the flow

as well as a more uniform vertical distribution within the pipe. The flows were also analyzed quantitatively using existing two-phase flow maps for horizontal and vertical flows. Generally, the horizontal two-phase flow map predictions disagreed with the recorded images because of the elevated flow pressures. The vertical flow map better predicted the flow regime, but still contained inconsistencies.

Turbine performance is presented in terms of shaft output torque and turbine efficiency as functions of rotational speed. The torque curves follow a linearly decreasing trend with increasing rotational speed, while the efficiency curves follow a parabolic trend with a maximum efficiency at moderate rotational speeds. Both the shaft output torque and the turbine efficiencies increase as the inlet pressure and inlet air mass fraction increase. The peak efficiency occurs at higher rotational speeds as air mass fraction and inlet pressure increase.

Anomalous performance behavior was observed at elevated inlet pressures with high air mass fractions. Within this range, the torque and efficiency were both suppressed. By preheating the process fluid, by use of an air heater and instant water heater, the torques and efficiencies were elevated to expected levels. This anomalous behavior is likely due to the formation of a 3rd phase (ice) within the Terry turbine as the water supplies heat to the expanding air. Otherwise, the Terry turbine generally follows expected performance trends.

9.1. Future Work

The Terry ZS-1 turbine, which was tested and reported on by Patil [25], will be tested using steam and water under similar pressures and gas mass qualities as the air-water

tests. This will allow for the development of a scaling relationship between the air-water tests and the steam-water tests. Additionally, a second scaling relationship between the aforementioned Terry ZS-1 turbine (1 nozzle, 18-inch wheel), and the Terry GS-2 turbine (5 nozzles, 24-inch wheel) used for this work will be developed to understand the scaling of parameters between the small-scale and full-scale system.

REFERENCES

[1] Kim, S. Il, Park, J. H., Ha, K. S., Cho, S.-W., and Song, J., 2016, "Analysis of Fukushima Unit 2 Accident Considering the Operating Conditions of RCIC System," Nucl. Eng. Des., **298**, pp. 183–191.

[2] 2018, "NRC: Reactor Core Isolation Cooling (RCIC) System," United States Nucl. Regul. Comm. [Online]. Available: https://nrcoe.inl.gov/resultsdb/SysStudy/RCIC.aspx. [Accessed: 29-Nov-2018].

[3] "Steam Turbines Power an Industry - Power Engineering" [Online]. Available: https://www.power-eng.com/articles/print/volume-100/issue-8/features/steam-turbines-power-an-industry.html. [Accessed: 21-Jan-2019].

[4] Dyson, C. W., 1909, "Test of Terry Steam Turbine," J. Am. Soc. Nav. Eng., **21**(3), pp. 884–890.

[5] 1985, *Emergency Feedwater Pump Turbine - Vendor Technical Manual*, Terry Steam Turbine Company.

[6] "Schutte & Koerting - Throttle Trip Valves" [Online]. Available: https://www.s-k.com/valves/throttle-trip-valves.cfm. [Accessed: 02-Sep-2019].

[7] Rahmeyer, W., Asce, A. M., and Driskell, L., *Control Valve Flow Coefficients*.

[8] Zhou, X.-M., Wang, Z.-K., and Zhang, Y.-F., 2017, "A Simple Method for High-Precision Evaluation of Valve Flow Coefficient by Computational Fluid Dynamics Simulation," Adv. Mech. Eng., **9**(7), p. 168781401771370.

[9] Bochnak, V. E., 1973, *Terry Wheel Water Slug Test*.

[10] Suzuki, H., Naitoh, M., Takahashi, A., Pellegrini, M., and Okada, H., 2014, "Analysis of Accident Progression with the SAMPSON Code in Fukushima Daiichi Nuclear Power Plant Unit 2," Nucl. Technol., **186**(2), pp. 255–262.

[11] Lopez, H., Erkan, N., and Okamoto, K., 2016, "Reactor Core Isolation Cooling System Analysis of the Fukushima Daiichi Unit 2 Accident with RELAP/ScdapSIM," J. Nucl. Sci. Technol., **53**(11), pp. 1899–1905.

[12] Lopez, H., Erkan, N., and Okamoto, K., 2016, "Two-Phase Flow Degradation on Fukushima-Daiichi Unit 2 RCIC Turbine Performance," J. Nucl. Sci. Technol., **53**(6), pp. 821–830.

[13] Li, G., Zhang, J., Qiu, B., Liu, M., and Yan, J., 2018, "MELCOR Modeling and Sensitivity Analysis of Fukushima Daiichi Unit 2 Accident Considering the Latest TEPCO Investigations," Ann. Nucl. Energy, **112**, pp. 364–373.

[14] Fernandez-Moguel, L., and Birchley, J., 2015, "Analysis of the Accident in the Fukushima Daiichi Nuclear Power Station Unit 3 with MELCOR_2.1," Ann. Nucl. Energy, **83**, pp. 193–215.

[15] Pellegrini, M., Suzuki, H., Mizouchi, H., and Naitoh, M., 2014, "Early Phase Accident Progression Analysis of Fukushima Daiichi Unit 3 by the SAMPSON Code," Nucl. Technol., **186**(2), pp. 241–254.

[16] Zhao, H., Zou, L., Zhang, H., and O'Brien, J. E., 2016, *Development and Implementation of Mechanistic Terry Turbine Models in RELAP-7 to Simulate RCIC Normal Operation Conditions*, Idaho Falls, ID (United States).

[17] Baker, O., 1954, "Simultaneous Flow of Oil and Gas," Oil Gas J., **53**(12), pp. 185–

195.

[18] Spedding, P. L., and Nguyen, V. T., 1980, "Regime Maps for Air Water Two Phase Flow," Chem. Eng. Sci., **35**(4), pp. 779–793.

[19] Hewitt, G. F., and Roberts, D. N., 1969, *Studies of Two-Phase Flow Patterns by Simultaneous X-Ray and Flash Photography*, Harwell, Berkshire.

[20] Yao, C., Dong, Z., Zhao, Y., and Chen, G., 2014, "The Effect of System Pressure on Gas-Liquid Slug Flow in a Microchannel," AIChE J., **60**(3), pp. 1132–1142.

[21] Zhao, Y., Chen, G., Ye, C., and Yuan, Q., 2013, "Gas–Liquid Two-Phase Flow in Microchannel at Elevated Pressure," Chem. Eng. Sci., **87**, pp. 122–132.

[22] Ozar, B., Brooks, C. S., Hibiki, T., and Ishii, M., 2013, "Interfacial Area Transport of Vertical Upward Steam–Water Two-Phase Flow in an Annular Channel at Elevated Pressures," Int. J. Heat Mass Transf., **57**(2), pp. 504–518.

[23] Ozar, B., Brooks, C. S., Euh, D. J., Hibiki, T., and Ishii, M., 2013, "Investigation of One-Dimensional Interfacial Area Transport for Vertical Upward Air–Water Two-Phase Flow in an Annular Channel at Elevated Pressures," Nucl. Eng. Des., **263**, pp. 362–379.

[24] Luthman, N., 2017, "Evaluation of Impulse Turbine Performance Under Wet Steam Conditions," M.S. Thesis, Department of Nuclear Engineering, Texas A&M University, College Station, TX.

[25] Patil, A., Wang, Y., Solom, M., Alfandi, A., Sundar, S., Vierow Kirkland, K., and Morrison, G., 2019, "Two-Phase Operation of a Terry Steam Turbine Using Air and Water Mixtures as Working Fluids," Appl. Therm. Eng., p. 114567.

[26] Patil, A., Sundar, S., Wang, Y., Solom, M., Kirkland, K. V., and Morrison, G., 2019, "Characterization of Steam Impulse Turbine for Two-Phase Flow," Int. J. Heat Fluid Flow.

[27] *IEC 60534-2-3: 2015 Industrial-Process Control Valves - Flow Capacity - Test Procedures*, International Standard.

[28] Kline, S. J., and McClintock, F. A., 1953, "Describing the Uncertainties in Single-Sample Exeriments," Mech. Eng., **75**(1), pp. 3–8.

[29] Stone, D., and Ellis, J., *Calibration and Linear Regression Analysis: A Self-Guided Tutorial*.

APPENDIX A INSTRUMENTATION AND CALIBRATION

Table 4: Equipment Locations and Calibrations

Sensor	Location in Facility	Accuracy
Pressure Transmitter Rosemount 0-300 PSIG	Air supply line 1	±0.04% of span
Pressure Transmitter Omega 0-250 PSIG	Air supply line 2	±0.08% of span
Differential Pressure Transmitter Rosemount 0-1000 in H_2O	TTV inlet to Turbine inlet	±0.04% of span
Pressure Transmitter Rosemount 0-300 PSIG	Turbine inlet	±0.04% of span
Pressure Transmitter Rosemount 0-150 PSIG	Turbine exhaust	±0.04% of span
Pressure Transmitter Rosemount 0-150 PSIA	Outlet piping	±0.04% of span
NI 9213 Module	DAQ	PASSED
NI 9205 Module	DAQ	PASSED
Load cell Omega 0-25 LBS; 0-100 LBS; 0-200 LBS	Dynamometer	Linearity: ±0.03% FSO
Gas Vortex Flowmeter Rosemount 0-30 ACFM	Air supply line 1	±0.75% of RD
Gas Turbine Flowmeter Omega 10-100 ACFM	Air supply line 1	±1% of RD
Gas Turbine Flowmeter Omega 25-250 ACFM	Air supply line 2	±1% of RD
Tachometer	Turbine	±1% RPM
Khrone Electromagnetic Flowmeter 0-134 GPM	Water line	±0.2% of reading
Water Turbine Flowmeter Omega 0-50 GPM	Water line	±0.91% of reading
Badger Electromagnetic Flowmeter 0-1 GPM	Water line	±0.11% of reading
Water Coriolis Flowmeter Rosemount 0-20 GPM	Water line	±0.10% of span (from manufacturer)

APPENDIX B UNCERTAINTY ANALYSIS

Sensors were calibrated to the project's required standard by external calibration facilities. The measurement uncertainty uses the Kline-McClintock method [28]. For example, the measurement uncertainty associated with the gas input power is

$$U_{P_{gas}} = \left[\left(\frac{\partial P_{gas}}{\partial p_{inlet}} U_{p_{inlet}}\right)^2 + \left(\frac{\partial P_{gas}}{\partial V_{inlet}} U_{V_{inlet}}\right)^2 + \left(\frac{\partial P_{gas}}{\partial p_{outlet}} U_{p_{outlet}}\right)^2\right]^{1/2}. \quad (9)$$

Uncertainty of the curve fit analysis for determination of flow coefficient parameters with air followed Stone's tutorial [29]. The random uncertainty for the valve testing parameters is included in the tabulated data in section 8.1 and 8.2. The random uncertainty for the turbine performance parameters at or above the BEP were within 3%. Below the BEP, uncertainty is within 8% as the turbine becomes difficult to control outside of the dynamometer's linear range. Table 5 shows the systematic uncertainties associated with the calculated parameters for valve flow coefficient and turbine performance.

Table 5: Maximum Systematic Uncertainty Associated to Desired Outcomes as a Percentage of Calculated Value

Outcomes	Systematic Uncertainty
Valve Flow Coefficient (Air)	1.6%
Valve Flow Coefficient (Water)	1.1%
Turbine Output Torque	1%
Turbine Efficiency	2%
Turbine Power Output	1%
Turbine Input Gas Power	1.9%
Turbine Input Liquid Power	1%